ISPRS Journal of Photogrammetry and Remote Sensing 216 (2024) 200–216

Contents lists available at ScienceDirect

ISPRS Journal of Photogrammetry and Remote Sensing

journal homepage: www.elsevier.com/locate/isprsjprs

Bark beetle pre-emergence detection using multi-temporal hyperspectral drone images: Green shoulder indices can indicate subtle tree vitality decline

Langning Huo [a,b,*], Niko Koivumäki [b], Raquel A. Oliveira [b], Teemu Hakala [b], Lauri Markelin [b], Roope Näsi [b], Juha Suomalainen [b], Antti Polvivaara [c], Samuli Junttila [c], Eija Honkavaara [b]

[a] Department of Forest Resource Management, Swedish University of Agricultural Sciences, 90 183, Umea, Sweden
[b] Department of Remote Sensing and Photogrammetry, Finnish Geospatial Research Institute, National Land Survey of Finland (NLS), 02150 Espoo, Finland
[c] School of Forest Sciences, University of Eastern Finland, 80101 Joensuu, Finland

ARTICLE INFO

Keywords:
European spruce bark beetle
Green attack
Early detection
Remote sensing
Hyperspectral imagery
Drone imagery

ABSTRACT

Forest stress monitoring and in-time identification of forest disturbances are important to improve forest resilience to climate change. Fast-developing drone techniques and hyperspectral imagery provide tools for understanding the forest decline process under stress and contribute to focused monitoring. This study explored and developed hyperspectral drone imagery for early detection of forest stress caused by European spruce bark beetle *Ips typographus* (L.), before offspring emergence, which is crucial in controlling the spread but has been shown to be challenging.

This study challenges the highest possible detectability of infested trees using a hyperspectral drone system that provided images with very high spectral, spatial, and temporal resolutions in Southern Finland. Images were acquired bi-weekly, four times (T1, T2, T3, T4), covering 8 weeks from trees being attacked by the first filial generation (F1) to the beginning of second filial generation (F2) brood emergence. Very low separability was observed for the reflectance from healthy and attacked trees, but the first and second derivative reflectance captured vitality changes, with the green shoulder region (wavelengths 490–550 nm) exhibiting the highest separability of all wavelengths (400–1700 nm). We discovered that the peak and valley values of the first and second derivative curves in the green shoulder region consistently shifted with longer infestation time.

Based on this finding, we developed green shoulder indices. The detection rates were 0.24–0.31 and 0.76–0.83 for T3 and T4, higher than commonly used VIs such as the Photochemical Reflectance Index and the Red Edge Inflection Position, with detection rates of 0.69 and 0.34 for T4, respectively. We also proposed simplified green shoulder indices using the reflectance from three bands that can be used with multispectral cameras and satellite images for large area monitoring of forest health. We concluded that the detectability of infestations was very low for the first month after attack, and then rapidly increased before brood emergence. We highlighted the great potential of green shoulder indices in quantifying the photochemical functioning of the vegetation under stress. The methodology can potentially be applied for early identification of forests with declining vitality caused by various sources of forest stress and disturbances, such as infestations, diseases and drought.

1. Introduction

Forest decline is becoming more frequent due to climate change (Pureswaran et al., 2018). Extreme weather events such as droughts and storms weaken forests and make them vulnerable to insect attacks. Forest insect disturbances have increased in frequency and magnitude, causing significant effects on the forest ecosystem, biodiversity, carbon cycle, and the timber industry (Battisti and Larsson, 2023; Pureswaran et al., 2018). European spruce bark beetle *Ips typographus* (L.) is one of the most devastating insects in Europe (Battisti and Larsson, 2023). It has significantly increased the mortality of Norway spruce Picea abies (L.), both in natural and managed forests. Huge financial losses have been estimated for the timber industry (Knoke et al., 2021) and the outbreaks also interfere with the sustainable use and management of

* Corresponding author at: Department of Forest Resource Management, Swedish University of Agricultural Sciences, 90 183, Umea, Sweden.
E-mail address: langning.huo@slu.se (L. Huo).

https://doi.org/10.1016/j.isprsjprs.2024.07.027
Received 23 April 2024; Received in revised form 25 July 2024; Accepted 26 July 2024
Available online 8 August 2024

forest resources long-term. Therefore, forest health monitoring and strategic damage control are needed for a climate-resilient industry. Forest digitalization and remote sensing techniques are under development to meet such needs, such as early detection of forest infestation, large-area mapping of damaged areas, forest predisposition evaluation, and environmental factor analysis of high-risk areas.

One of the critical questions in forest remote sensing is how early infestations can be identified using remote sensing data (Marvasti-Zadeh et al., 2024; Estrada et al., 2023). Such technical development is driven by the need to remove infested trees from the forest before the emergence of the next bark beetle generation to prevent the spread and reduce the population of the bark beetle (Dobor et al., 2020), since logging after this critical period has been shown to have minimal impact on bark beetle dynamics and forest damage level (Dobor et al., 2020; Fora and Balog, 2021). The overwintered bark beetles attack trees in the spring and lay eggs in the phloem. The developmental time from egg to imago is determined by the temperature e.g. 8–15 weeks as shown in a study in Sweden from 2006 to 2010 (Öhrn et al., 2014a, 2014b), with shorter development times occurring in warmer areas (Wermelinger, 2004). Another study in Sweden recorded swarming from the new generation starting 10 weeks after the initial attack in 2021 (Huo et al., 2023). Therefore, detecting infested trees within such a time is the target, with the feasibility of this having been investigated in many studies (Marvasti-Zadeh et al., 2024; Zabihi et al., 2021). This critical period is also often called the green attack phase because most infested trees stay green without visible crown changes during this time.

Pre-emergence or green attack detection has been shown to be very challenging, even with specialized remote sensing data, which has the capability to reveal subtle pigment and physiological changes in plants (Marvasti-Zadeh et al., 2024; Estrada et al., 2023; Zabihi et al., 2021; Luo et al., 2022). When using satellite images, the resolution is often the limiting factor and the small number of infested trees(Kärvemo et al., 2023; Persson et al., 2024) relative to large pixels makes it challenging to differentiate forests in the early stages of infestation from healthy ones (Bárta et al., 2021; Huo et al., 2021; Dalponte et al., 2023; Jamali et al., 2023; Olsson et al., 2023; Abdullah et al., 2019). When using images with resolution lower than the crown radius, the spectral signals can be affected by the forest structure, forest floors, and even forest vitality and vulnerability. Although spectral differences can be significant between healthy forests and forests in the early stages of infestation, those differences often exist before attacks (Bárta et al., 2021; Trubin et al., 2023; Huo et al., 2021), implying high false positive estimations when implementing the methods on an unknown area at an unknown time. Overfitting is also an issue for implementation when using complex machine learning structures and many variables with data that derive from a small sample (Huo et al., 2023).

Drone images and airborne images can have a high resolution (e.g. $\leq$ 0.5 m) and therefore support spectral analysis focusing on the tree crown with less influence from the surrounding trees and canopy gaps. Using airborne and drone imagery, trees whose vitality is declining can be detected and mapped with high accuracy (Fassnacht et al., 2014; Junttila et al., 2022; Safonova et al., 2022; Turkulainen et al., 2023). However, studies focusing on pre-emergence detection have rarely been undertaken, or have had relatively low accuracy. To date, only four studies have quantified the detectability of green attacks using drone imagery (Huo et al., 2023; Minařík et al., 2021; Honkavaara et al., 2020; Bárta et al., 2022). From those studies, a good methodology was developed to quantify the detectability of green attacks according to the duration of infestation (Huo et al., 2023). Using multispectral drone images, the detectability after the first five weeks of infestation was very low, while it was sufficient at 10 weeks of infestation and twice the detectability of the field inventory based on discoloration. However, this study also pointed out that the F1 filial generation started 10 weeks after the first swarming, illustrating the need to detect infestation earlier for damage control (Huo et al., 2023). Compared to multispectral imagery, hyperspectral imagery can capture reflectance in much narrower bands, covering a broader range of wavelengths. Therefore, it has the potential to enhance pre-emergence detection (Honkavaara et al., 2020).

Previous studies using hyperspectral images still relied on the selection of vegetation indices (VIs) based on experiences with multispectral images or other plant stress scenarios, while the potential offered by an expanded spectral range and diverse hyperspectral vegetation indices still remains unexplored. For example, two studies found the Photochemical Reflectance Index (PRI) has similar good sensitivity as Red Edge Inflection Position (REIP), but the potential of PRI was not highlighted (Bárta et al., 2022; Einzmann et al., 2021). Studies carried out using hyperspectral imagery on stressed crops under controlled conditions such as nitrogen limitation, drought, poisoning, and diseases (Peñuelas et al., 1994; Zahir et al., 2022; Zhang et al., 2019), have demonstrated the capability of hyperspectral characteristics to indicate physiological changes. Thus, we assumed that high-resolution hyperspectral images would provide better detection than other sources of optical data and, if not, that there would be a low probability of success using other optical data.

To test this assumption, we carried out studies to quantify the detectability range, using multi-temporal hyperspectral drone images with 448 bands covering 400–1700 nm with 0.1 m resolution. The overall objectives were (1) quantifying the detectability of infested trees depending on the duration of infestation, (2) carrying out a comprehensive comparison of the separability of the full wavelength range and finding spectral indicators of the duration of infestation. For a robust performance, the indicators should: (a) show little difference between healthy and attacked trees before infestation, (b) continuously increase/decrease with longer duration of infestation, and (c) be less affected by phenology i.e. show little fluctuation over time for healthy trees. In addition, (3) we aimed to propose simplified spectral indicators that were feasible for multispectral sensors to reduce the potential operational cost of using hyperspectral cameras. For this study, we first investigated the separability of each spectral band and the derivatives and then focused on the green region that showed the highest potential in the separability analysis. Further investigation of the red edge, NIR, and SWIR bands is planned for future studies.

2. Materials

2.1. Test area and sample trees

The test area was located in Helsinki city central park (60°15′25.200″N, 24°55′19.200″E, Fig. 1). The area is dominated by mature Norway spruce trees and is known to have ongoing infestation by *I. typographus*. An area of 20 ha was selected for the remote sensing study. The temperature data were obtained from the nearest weather station (6 km from the field site), and the daily thermal sum (dd) since 1 April was calculated, using 5° as the base temperature, to indicate the swarming time and development of bark beetles (Fig. 1f). From 11 July 2021 (week 27) to 24 July 2021 (week 29), the thermal sum was between 800 and 1000 dd, which indicated the peak time of the F1 filial generation swarming and attacks. Nine weeks later, on 11 September 2021 (week 36), the temperature sum reached 1500 dd, indicating the F2 filial beetle was fully developed and starting to overwinter under barks or underground (Öhrn et al., 2014b; Annila, 1969). This study focused on the early detection of the infestation by the F1 filial generation and tested the detectability before the beginning of the filial beetle emergence in week 36.

Tree health data were collected by experts in field surveys on 6–9 September 2021. Various symptoms were evaluated and classified visually on a discrete numerical scale representing the severity of the symptom (Table 1). The health data were recorded for individual spruce trees dispersed throughout the area, with the aim of having a uniform distribution of different health statuses (Junttila et al., 2022). The positions of the trees were obtained from orthophotos collected before fieldwork. The recorded health symptoms were crown color, defoliation,

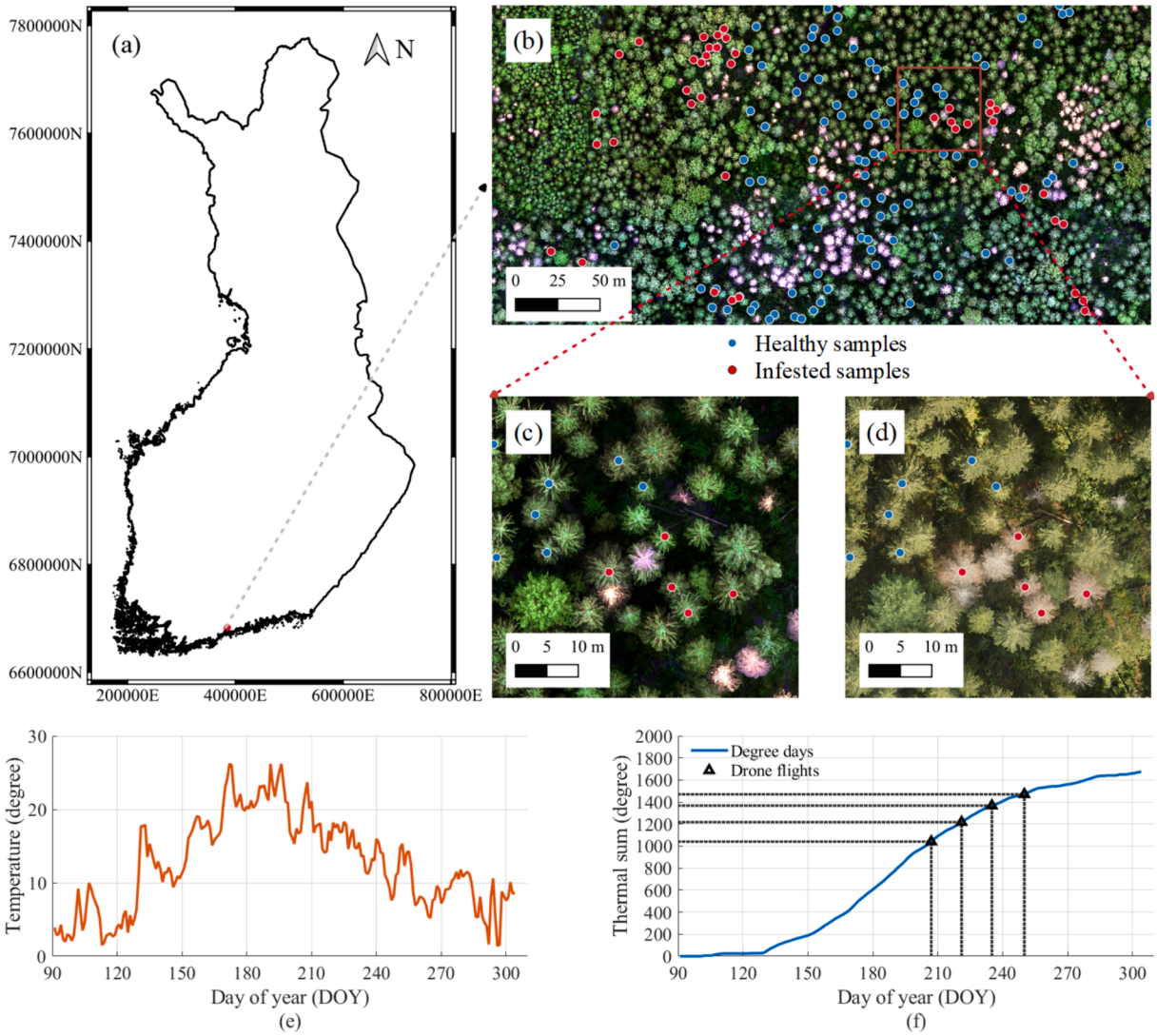

Fig. 1. (a) Study area in southern Finland, (b–d) the plots shown on RGB orthophotos, (e) the temperature, and (f) thermal sum. (b) Healthy and infested trees shown on an RGB orthophoto acquired on 7 September 2021. (c–d) Examples of healthy and trees suffering green attack in the RGB images acquired on 7 September 2021 (c) and 21 June 2022 (d). (For interpretation of the references to color in this figure legend, the reader is referred to the web version of this article.)

Table 1
Camera settings during the flights.

Camera setting	AFX10 VNIR	AFX17 SWIR
Spatial: Binning; pixels	1; 1024	1; 640
Spectral: Binning; bands	2; 224	1; 224
FPS; Exposure time (ms)	71.72; 13.69	35.845; 13.94
Flight speed (m/s)	7	7
Flight height (m)	100	100
GSD (cm): tree tops, ground	5.6, 7	8, 10

resin flow, bark damage, and decreased canopy height. The scoring was 0–5 for the crown color, 0–4 for defoliation, and 0–2 for resin flow and bark damage.

The healthy and infested trees during F1 filial generation swarming were selected as samples according to the field data and visual interpretation using RGB orthophotos acquired on 7 September 2021 and 21 June 2022. The healthy trees without any symptoms (i.e. scoring 0) were selected from the field data, and the ones with visible discoloration on the orthophoto acquired on 7 September 2021 were excluded, resulting in 56 healthy trees used as samples. Trees attacked by the F1 filial generation were usually green without discoloration during the first six weeks of infestation and appeared dead with red or grey crowns in the following summer. Based on this criteria, 41 trees were identified as attacked by the F1 filial generation i.e. without discoloration on 7 September 2021, and appearing to be dead on 21 June 2022.

2.2. Remote sensing datasets

The DJI Matrice M600 hexacopter drone was employed as the platform for the two pushbroom hyperspectral cameras, Specim AFX10 VNIR and AFX17 SWIR cameras, flown in separate flights (Fig. 2). The cameras were mounted on a Gremzy T7 gimbal weighing 1.86 kg and having a payload of 3.175 kg. The Specim AFX hyperspectral cameras integrated a computer and a high-end GNSS/IMU unit. The AFX10 VNIR camera (2.1 kg, 400–1000 nm, spectral binning of 2) had a spectral resolution of 5.5 nm, a spectral sampling of 2.68 nm, 224 bands, 1024 spatial pixels, and a 15 mm focal length. The AFX17 SWIR camera (2.4 kg, 900–1700 nm, no spectral binning) had a spectral resolution of 8 nm, a spectral sampling of 3.5 nm, 224 bands, 640 spatial pixels, and an 18 mm focal length (Specim, 2022). Details of the camera settings are given in Table 1. Determined by the sensors used, this study references the spectral region as:

Fig. 2. Specim AFX10 VNIR camera onboard the DJI Matrice 600 Pro hexacopter drone.

- Visible bands, covering blue, green, red bands (400–670 nm)
- Red edge bands, covering 670–780 nm
- NIR bands, covering 780–1100 nm
- SWIR bands, covering 1100–1350 nm (SWIR1) and 1500–1700 nm (SWIR2).

Time series of hyperspectral VNIR and SWIR images were collected during the summer of 2021, when the F1 filial generation of *I. typographus* was swarming. Altogether, four flights were carried out from 26 July to 7 September 2021 (Table 2). The hyperspectral images were acquired at weeks 30, 32, 34, and 36 of the year and the thermal sum was 1041 dd, 1217 dd, 1367 dd, and 1470 dd, respectively (Fig. 1f), indicating the trees were in the early infestation stage before F2 brood emergence. In the following sections, we denote the time of the four image acquisition flights as T1, T2, T3, and T4. The flights were carried out approximately 100 m above ground level using the same flight plan every time for the AFX 10 and 17 cameras. The area was covered with eight flight lines of length 200–240 m; the flight lines were planned with side overlaps of 36 % at ground level and 20 % at treetops. The flight speed was 7 m/s. Details of camera settings during flights are given in Table 1 and flight condition information during each campaign is shown in Table 2.

Table 2
Flight details.

Date	Camera	UTC Time*	Sun zenith	Sun azimuth	Illumination conditions
26 July 2021	AFX10 VNIR	07:31–07:42	51°	123°	Sunny (uniform)
26 July 2021	AFX17 SWIR	08:00–08:11	48°	131°	Sunny (uniform)
09 August 2021	AFX10 VNIR	08:31–08:46	49°	142°	Cloudy (quite uniform)
09 August 2021	AFX17 SWIR	10:10–10:25	45°	175°	Cloudy (quite uniform)
23 August 2021	AFX10 VNIR	07:15–07:26	60°	123°	Varying
23 August 2021	AFX17 SWIR	08:49–09:00	52°	150°	Varying
07 September 2021	AFX10 VNIR	07:40–07:50	62°	134°	Sunny (uniform)
07 September 2021	AFX17 SWIR	10:03–10:12	54°	175°	Sunny (uniform)

* Local time was UTC+03 h.

The hyperspectral AFX10 VNIR and AFX17 SWIR datasets were georectified using the Specim CaliGeoPRO v2.3.12 software. The post-processed kinematic (PPK) GNSS/IMU solutions were calculated for the flight trajectories using the Applanix PosUAV v 8.6 software. The GNSS base station data were obtained from the National Land Survey FINPOS service using the virtual reference station method. A digital surface model (DSM) collected in the summer of 2021 with a GSD of 1 m and smoothed with a Gaussian filter was used in the georectification phase. The boresight calibration was carried out in a signalized test field. The orthophotos were sampled with a 10 cm GSD. The raw image pixel values of AFX datasets were transformed to the units of radiance using the Specim CaliGeoPRO v2.3.12 software. The radiance images were transformed to reflectance data using the empirical line method by forcing the line to cross the y-axis at point (0,0) and determining the slope by using a panel with 25 % nominal reflectance.

3. Methods

This study had four stages. Sections 3.1 and 4.1 describe the evaluation of the crown segmentation and reflectance calculation. Sections 3.2 and 4.2 describe finding the spectral region and wavelengths with the highest potential for indicating infestation. In Sections 3.3 and 4.3, we describe the characterization of the green shoulder spectrum using peak and valley values from the spectral curves, and present how they shift over time during infestation. Green shoulder indices were constructed and simplified, and their performance was compared with other VIs, as described in Sections 3.4 and 4.4.

3.1. Crown segmentation and reflectance calculation

Tree crowns were automatically segmented from orthomosaics using a marker-controlled watershed algorithm, as described in Huo et al. (2023). A single band of the orthomosaic (e.g. wavelengths 553 nm and 1109 nm from AFX10 VNIR and AFX17 SWIR, respectively) was first used to make a segmentation mask, which was then applied to every band. To make the segmentation mask, pixels with the maximum pixel values from a smoothed single-band image were used as the markers, and then a marker-controlled watershed segmentation was carried out using the SegmentTrees tool in the Lidar Toolbox in Matlab (MathWorks, Inc., 2021). We derived individual tree crown images after these steps, with the markers as the tree tops (Fig. 3). The health status of the trees shown in each image was determined by matching the markers and the location of field data. In this way, tree crowns were segmented from all orthomosaics acquired by the two cameras at four different times. During this process, not all trees were successfully segmented from all the images due to areas with low side overlap, undersegmentation, or tree crowns that were too small. This study focused on the time series spectral changes during tree vitality decline, thus, only the trees successfully segmented from all eight images were used as samples, and their spectral reflectance data were further analyzed. The reflectance of each tree was calculated by averaging 75 % of the brightest pixels (determined in a sensitivity analysis). To match the spectrum from different times, the spectra were all normalized using the Frobenius norm, which is the square root of the sum of squares of reflectance values in the full spectra (Meurant, 1999). The spectral curves were also smoothed using Savitzky-Golay smoothing with polynomial order 2 and frame length 7.

3.2. Spectral signatures and sensitive bands

We analyzed the normalized and smoothed spectral values (denoted as reflectance in the following sections) and their first and second derivatives (denoted as 1st and 2nd derivatives, Eq. (1) and Eq. (2). Derivative analysis techniques were developed for spectroscopy during 1990 s, which have been shown to be less sensitive to illumination changes caused by sun angle and topography (Tsai and Philpot, 1998). A

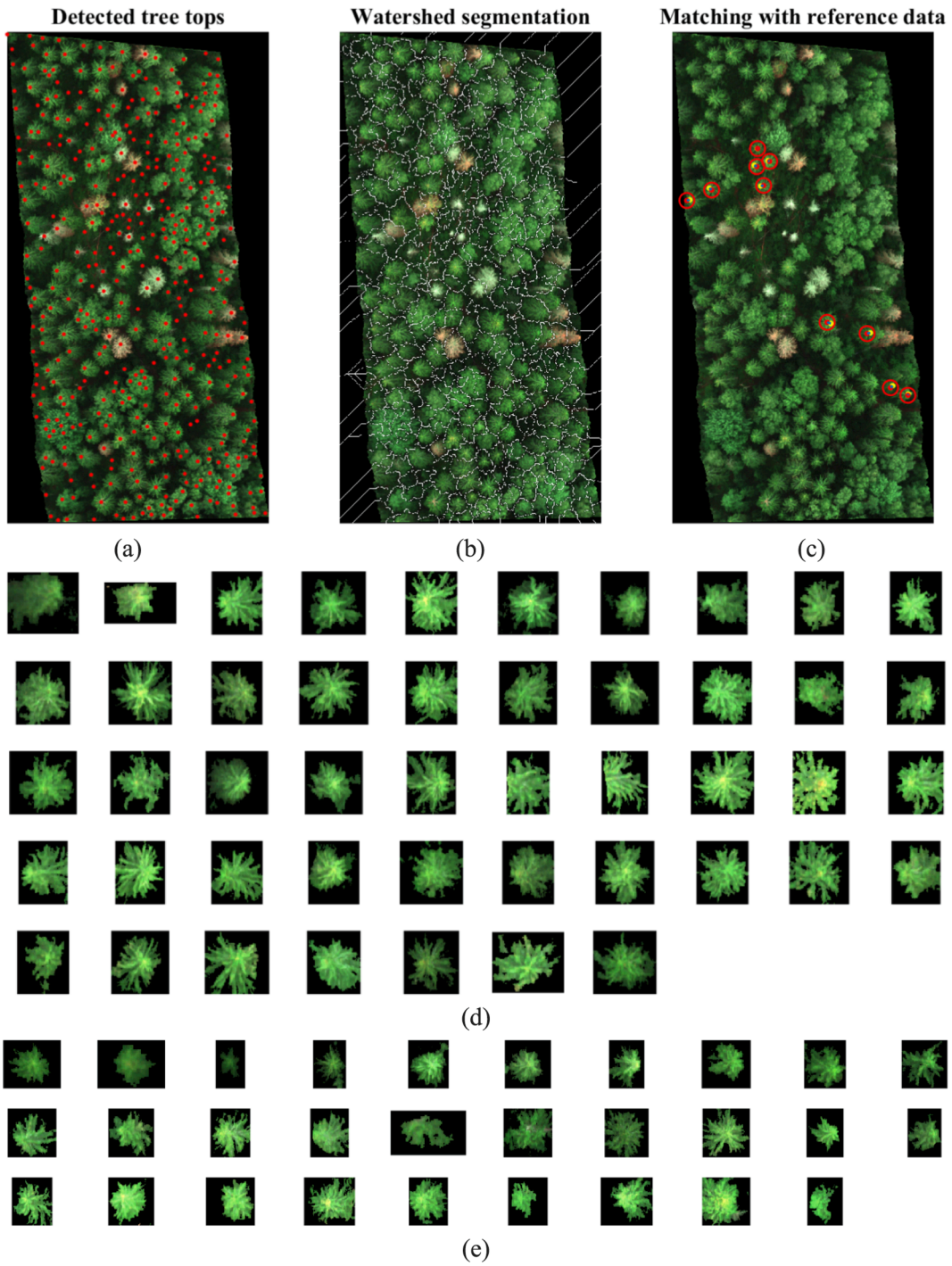

Fig. 3. An example of tree crown segmentation including (a) local maximum detection, (b) watershed segmentation, (c) matching with reference data, and crown segments of (d) healthy and (e) infested trees.

1st derivative describes the slope of a reflectance curve at a certain wavelength, while a 2nd derivative describes the curvature of the reflectance curve.

$$R' = \frac{dR}{dW} = \frac{Reflectance_{band i+1} - Reflectance_{band i}}{Wavelength_{band i+1} - Wavelength_{band i}} \quad (1)$$

$$R'' = \frac{d2R}{dW2} = \frac{d}{dW}\left(\frac{dR}{dW}\right) \quad (2)$$

At each point during the infestation, reflectance, 1st and 2nd derivatives between healthy and attacked trees were compared. Bands with significant differences between the two groups at $p < 0.01$ level were highlighted using a two-sided Wilcoxon rank-sum test. The separability between the two groups at each band and each time was quantified using a linear discriminant analysis (LDA) and labeled with the kappa coefficient of the LDA classification.

As a good indicator of the infestation stage should consistently increase or decrease as vitality declines, we considered bands with increasing separability over time as sensitive bands. We aimed to find the bands that responded to the infestation and further develop indices using those responsive bands.

3.3. Green shoulder spectrum

3.3.1. Green shoulder Inflection Point and green shoulder curvature point

Healthy plants usually have high chlorophyll content and, thus, the spectral signature has high absorption in the red and blue regions. When under stress, photosynthesis is limited, resulting in a decrease in the chlorophyll content (Abdullah et al., 2018; Li et al., 2022). For some plants, the carotenoid content increases to protect the plant from damage caused by excessive light or free radicals, so there is less absorption in the green shoulder region (500–550 nm) of the spectrum (Vilfan et al., 2018). Xanthophylls, a class of pigments that belong to the carotenoid group, help in dissipating excess light energy absorbed by chlorophyll during photosynthesis under healthy conditions. Under stress, their concentration increases and the xanthophyll cycle may shift involving the interconversion of xanthophyll pigments, contributing to photoprotection and antioxidant defense (Peguero-Pina et al., 2008). Certain nutrient deficiencies can also lead to an increase in anthocyanin production, which commonly has absorption peaks in the range of 490 to 560 nm (Latowski et al., 2011).

Therefore, we first focused on the spectral changes due to infestation in the blue-green region (490–560 nm), denoted as the green shoulder region. In this region, the reflectance increases with longer wavelengths, showing two peaks on the 1st derivative curve at approximately 520 nm and 545 nm, and one valley on the 2nd derivative curve at approximately 530 nm. In this study, we denoted them as Green Shoulder Inflection Points (GSIPs) and Green Shoulder Curvature Points (GSCPs) (Fig. 4, Table 3). We made scatter plots of the GSIPs and GSCPs to show the differences between healthy and infested trees, and how they changed over time.

3.3.2. Green shoulder indices from hyperspectral curves

Based on the results in 3.3.1, we proposed two green shoulder indices, as given by Eqs. (3) and (4),

Green Shoulder Curvature Ratio 1

$$GSCR1 = \frac{\mathrm{GSIP}_{545}}{-\mathrm{GSCP}_{530}} \tag{3}$$

Green Shoulder Curvature Ratio 2

$$GSCR2 = \frac{\mathrm{GSIP}_{545}}{\mathrm{GSIP}_{520} \times (-\mathrm{GSCP}_{530})} \tag{4}$$

To show the changes over time, we also calculated the index change by comparing it to the first image acquired at T1, as

$$\delta VI = \left| \frac{(\delta VI_{Ti} - \delta VI_{T1})}{\delta VI_{T1}} \right| \tag{5}$$

where δ VI refers to the tested indices GSIP_{545}, GSCP_{530}, GSCR1, GSCR2, and Ti refers to the image acquired at Ti. These four tested indices should be stable for healthy trees over time while increasing with longer durations of the infestation.

Table 3
Abbreviation and calculation of the green shoulder indices.

Abbr.	Term	Calculation
GSIP	Green Shoulder Inflection Point	The point of maximum slope on the reflectance spectrum in the green shoulder range (490–560 nm), where the 1st derivatives show peak values at approx. 520 nm and 545 nm.
GSIP_{520}	1st derivative of GSIP at approx. 520 nm	
GSIP_{545}	1st derivative of GSIP at approx. 545 nm	
GSCP	Green Shoulder Curvature Point	The point of maximum curvature on the reflectance spectrum in the green shoulder range (490–560 nm), where the 2nd derivatives show valley values at approx. 530 nm.
GSCP_{530}	2nd derivative of GSCP at approx. 530 nm	

3.3.3. Simplified green shoulder indices

We investigated simplified green shoulder indices using multiple spectral bands instead of derivative curves. This approach can enable detection using multispectral cameras rather than hyperspectral cameras, which are more expensive and require heavy-lift drones for data acquisition.

We proposed a Green Shoulder Stress Index (GSVI, Eq. (6) and assumed that it had a linear relationship with GSCP_{530} (Eq. (7). GSCP_{530} describes the curvature of the reflectance curve at wavelength approximately 530 nm i.e. the reflectance difference between 530 nm and the average reflectance of 560 nm and 490 nm. GSIP_{520} and GSIP_{545} describe the slopes of the reflectance curve at wavelengths approximately 520 nm and 545 nm, thus we assumed GSIP_{520} had a linear relationship with the reflectance difference between 530 nm and 490 nm (Eq. (8), and assumed GSIP_{545} had a linear relationship with the reflectance difference between 560 nm and 530 nm (Eq. (9). GSCR1 and GSCR2 were obtained using the combination of GSCP_{530}, GSIP_{520} and GSIP_{545}, and thus linear relationships were assumed, as shown in Eqs. (10) and (11).

$$GVSI = \frac{R_{550} + R_{490}}{2} - R_{530} \tag{6}$$

$$GSCP_{530} = \alpha 1 GVSI + \beta 1 = \alpha 1 \left(\frac{R_{550} + R_{490}}{2} - R_{530} \right) + \beta 1 \tag{7}$$

$$GSIP_{520} = \alpha 2 (R_{530} - R_{490}) + \beta 2 \tag{8}$$

$$GSIP_{545} = \alpha 3 (R_{550} - R_{530}) + \beta 3 \tag{9}$$

$$GSCR1 = \alpha 4 \left(\frac{R_{550} - R_{530}}{-GVSI} \right) + \beta 4 = \alpha 4 \left(\frac{R_{550} - R_{530}}{-\left(\frac{R_{550}+R_{490}}{2} - R_{530} \right)} \right) + \beta 4 \tag{10}$$

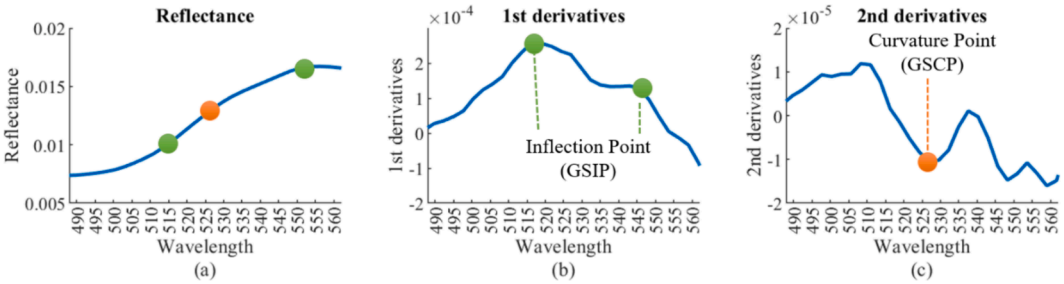

Fig. 4. Illustration of the Green Shoulder Inflection Point and Green Shoulder Curvature Point on the spectral curves. (For interpretation of the references to color in this figure legend, the reader is referred to the web version of this article.)

$$GSCR2 = \alpha 5\left(\frac{R_{550}-R_{530}}{(R_{530}-R_{490})\times\left(-\left(\frac{R_{550}-R_{490}}{2}-R_{530}\right)\right)}\right)+\beta 5 \quad (11)$$

where R_{490}, R_{530}, and R_{560} are the reflectance, and α and β are the coefficients of the linear relationship. When the linear relationships were confirmed in Eqs. (6)–(11), the GSCR indices could be simplified from Eqs. (10) and (11) without the coefficients, only using the reflectance of three bands, $Blue_{490}$, $Green_{530}$, and $Green_{560}$ (Eqs. (12) and (13):

$$GSCR1_{MS} = \frac{R_{550}-R_{530}}{R_{530}-\frac{R_{550}+R_{490}}{2}} \quad (12)$$

$$GSCR2_{MS} = \frac{R_{550}-R_{530}}{(R_{530}-R_{490})\times\left(R_{530}-\frac{R_{550}+R_{490}}{2}\right)} \quad (13)$$

$GSCR1_{MS}$ and $GSCR2_{MS}$ were calculated for the healthy and infested trees from images T1 to T4, and δ $GSCR1_{MS}$ and δ $GSCR2_{MS}$ were calculated (Eq. (5) and evaluated using the same evaluation method as described in 3.3.2.

3.4. Detection evaluation and comparing VIs

Twenty additional VIs were selected and tested (Table 4) to compare the performance with the green shoulder indices. The tested VIs included VIs 1–6 constructed using visible bands that are sensitive to pigments, VIs 7–13 constructed using visible and red edge bands, VIs 14–16 constructed using red edge bands that are sensitive to plant stress, and VIs 18–20 constructed using SWIR bands that are sensitive to water content.

The detection performance of early infestation using a single VI was quantified with two dimensions in this study: (1) the separability of healthy and infested trees from each specific time data, T1, T2, T3, or T4, quantified using the kappa coefficient of a linear discriminant analysis (LDA) applied to healthy and infested groups. LDA calculates the mean and covariance parameters of the two classes based on probability density functions and determines a threshold to predict points from the second class if the log of the likelihood ratios is bigger than the threshold. Therefore, the classification accuracy (kappa coefficient) could be used to quantify how much two groups overlapped and how well they can be separated. Separability was denoted when using this method, and it represented how well the healthy and infested trees could be separated at a specific time under supervised classification. (2) Detectability, or detection rate, was calculated using images from all acquisitions i.e. T1 + T2 + T3 + T4. We first calculated the 1 % or 99 % percentile VI values (Th_{VI_i}) for the healthy trees at all times T1 to T4, and defined the range as a 'healthy range'. Among the infested trees, the ones with VI_i outside this range were considered to be detectable and a proportion of them treated as 'detectability'. Detectability represented how well the infested trees could be identified by unsupervised classification i.e. using empirical thresholds.

The performance of all VIs in this study (including the new ones proposed) was represented by both separability and detectability. A vegetation index sensitive to phenology or illumination conditions might result in high separability in a single image but low detectability, as the values of healthy trees were not stable from different images. We aimed to find and construct indices less sensitive to phenology, showing high separability and high detectability.

Table 4
Details of the vegetation indices (VIs) used.

No.	Abbr.	Name	Definition for Sentinel-2 bands (https://www.indexdatabase.de/)	References
1	PRI 531/570	Photochemical Reflectance Index	$\frac{R_{531}-R_{570}}{R_{531}+R_{570}}$	(Peñuelas et al., 1994)
2	PRI 550/530	Photochemical Reflectance Index	$\frac{R_{550}-R_{530}}{R_{550}+R_{530}}$	(Peñuelas et al., 1994)
3	NGRDI	Normalized Green-Red Difference Index	$\frac{R_{550}-R_{665}}{R_{550}+R_{665}}$	(Tucker, 1979)
4	GLI	Green Leaf Index	$\frac{(R_{550}-R_{665})+(R_{550}-R_{490})}{(R_{550}+R_{665})+(R_{550}+R_{490})}$	(Louhaichi et al., 2001)
5	CIG	Chlorophyll Index Green	$\frac{R_{865}}{R_{550}}-1$	(Gitelson et al., 2003)
6	NDVI	Normalized Difference Vegetation Index	$\frac{R_{865}-R_{550}}{R_{865}+R_{550}}$	(Rouse et al., 1973)
7	CVI	Chlorophyll Vegetation Index	$\frac{R_{865}\times R_{705}}{R_{550}\times R_{550}}$	(Vincini et al., 2008)
8	ARI	Anthocyanin reflectance index	$\frac{1}{550nm}-\frac{1}{700nm}$	(Anatoly A. Gitelson et al., 2001)
9	GNDVI	Green Normalized Difference Vegetation Index	$\frac{R_{780}-R_{550}}{R_{780}+R_{550}}$	(Gitelson et al., 1996)
10	MR-DSWI1	Multiple Ratio Disease–Water Stress Index 1	$\frac{R_{705}\times R_{705}}{R_{550}\times R_{783}}$	(Huo et al., 2023)
11	MR-DSWI2	Multiple Ratio Disease–Water Stress Index 2	$\frac{R_{705}\times R_{705}\times R_{865}}{R_{550}\times R_{783}\times R_{783}}$	(Huo et al., 2023)
12	MR-DSWI3	Multiple Ratio Disease–Water Stress Index 3	$\frac{R_{705}\times R_{705}\times R_{665}}{R_{550}\times R_{783}\times R_{550}}$	(Huo et al., 2023)
13	MR-DSWI4	Multiple Ratio Disease–Water Stress Index 4	$\frac{R_{705}\times R_{705}\times R_{865}\times R_{665}}{R_{550}\times R_{783}\times R_{783}\times R_{550}}$	(Huo et al., 2023)
14	NDRE	Normalized Difference Red Edge Index	$\frac{R_{790}-R_{720}}{R_{790}+R_{720}}$	(Barnes et al., 2000)
15	RVSI	Red Edge Vegetation Stress Index	$\frac{R_{718}+R_{748}}{2}-R_{733}$	(Merton, 1998)
16	REIP	Red Edge Inflection Point (linear interpolation)	$700+40\times\left(\frac{\frac{R_{670}+R_{780}}{2}-R_{700}}{R_{740}-R_{700}}\right)$	(Guyot et al., 1988)
17	DRS	Difference Red & SWIR	$\sqrt{{R_{665}}^2+{R_{1610}}^2}$	(Huo et al., 2021)
18	NDII	Normalized Difference Infrared Index	$\frac{R_{819}-R_{1649}}{R_{819}+R_{1649}}$	(Hardisky et al., 1983)
19	NDWI	Normalized Difference Water Index	$\frac{R_{857}-R_{1241}}{R_{857}+R_{1241}}$	(Jackson et al., 2004)
20	MSI	Moisture Stress Index	$\frac{R_{1600}}{R_{820}}$	(HUNTJR and ROCK, 1989)

4. Results

4.1. Crown segmentation

After individual trees were segmented, 47 healthy and 29 infested trees were successfully segmented from both AFX10 VNIR and AFX17 SWIR images on all four revisited images (Table 5). Images of these 76 trees were used for further analysis and their spectral signatures are given in Fig. 5. Several small trees close to deciduous trees were not successfully segmented due to under-segmentation.

Table 5
Number of sample trees and segmented trees from the images.

Data resource	Number of trees (Segmentation rates)	
	Healthy	Infested
Trees with health records from the field and RGB images	56	41
Segmented from AFX10 VNIR image at T1	53 (95 %)	40 (98 %)
Segmented from AFX17 SWIR image at T1	52 (93 %)	37 (90 %)
Segmented from AFX10 VNIR image at T2	52 (93 %)	39 (95 %)
Segmented from AFX17 SWIR image at T2	56 (100 %)	36 (88 %)
Segmented from AFX10 VNIR image at T3	55 (98 %)	39 (95 %)
Segmented from AFX17 SWIR image at T3	54 (96 %)	34 (83 %)
Segmented from AFX10 VNIR image at T4	55 (98 %)	38 (93 %)
Segmented from AFX17 SWIR image at T4	56 (100 %)	39 (95 %)
Number of trees segmented from all above eight images	47 (84 %)	29 (71 %)

4.2. Spectral signatures and sensitive bands

4.2.1. Reflectance curves

The crown reflectance of each wavelength was first compared between healthy and infested trees at T1, T2, T3, and T4 (Fig. 6). At T1, the healthy and infested trees showed no significant difference at any wavelength. The visible bands (400–670 nm) did not show significant differences between the two groups until T4 when differences were observed between 600 and 650 nm. Within the red edge range (670–780 nm), reflectance data around 760 nm first showed significance at T3 and most of them were significantly different at T4. Several spectral bands from 1000 to 1580 nm were significant at T2 but not at later infestation stages, except for the bands 1120–1170 nm which were significant in T2 and T3, and bands 1320–1340 nm which were significant in T2, T3 and T4. As hyperspectral reflectance data are sensitive to many factors other than physiological properties, such as branch structures and light conditions during data acquisition, we only focused on the spectral bands showing increasing separability between healthy and infested trees.

The separability of the reflectance between healthy and infested trees showed how much the two groups overlap and the possibility of separating them with a single threshold. We plotted the separability of each band at each time, and marked the wavelengths with increasing separability over time (Fig. 6 b1–b4), indicating the infestation stages. The bands with increasing separability over time included wavelengths around 800 nm with the highest separability at T4, followed by bands around 700 nm, 600 nm, and 1000 nm, which showed higher separability at T3 than 800 nm. The SWIR bands around 1300 nm and 1500 nm also showed significant differences or relatively high separability at T2, T3, or T4, but the separability did not consistently increase over time. SWIR bands with wavelengths $>$ 1500 nm showed good separability at T1, T2, and T4, but no separability at T3.

4.2.2. First derivative reflectance curves

Using the same analysis method, we showed how the 1st derivatives corresponded to the infestation over time (Fig. 7). Of the bands showing increasing separability between healthy and infested trees, the band 552 nm showed the highest separability of 0.23, 0.44, 0.53, and 0.67 at T1, T2, T3, T4, respectively. The separability was also higher than the reflectance separability in 4.2.1. However, proven separability at T1 implied sensitivity to factors other than an infestation, as the health of attacked trees usually does not decline immediately after the attack. Bands with wavelengths around 722 nm also had high separability of 0.40, 0.49, and 0.58 at T2, T3, T4, respectively, but 0 at T1. Bands with wavelengths around 800 nm also showed increasing separability but the separability was not as high as those for 552 nm and 722 nm. Using derivative analysis, some bands in the SWIR region showed increasing separability, and bands with wavelengths around 1650 nm showed relatively high separability (0.46) at T4.

4.2.3. Second derivative reflectance curves

The 2nd derivative curves are shown with wavelengths marked as significant differences between the healthy and infested trees (Fig. 8). Two peaks of separability were found, one peak at 530 nm, which had the highest separability of 0.71 at T4, and the other peak at 715 nm with separability of 0.65 for that week. At T2 and T3, the separability was higher at 715 nm than at 530 nm, however, at T1, the separability was 0.24 at 715 nm while 0 at 530 nm. As the attacked trees should show little effect from the bark beetle colorization at 1–3 weeks of infestation, we considered lower detectability at T1 to be more reasonable. In addition, the separability at 530 nm increased the most over time i.e. 0.00, 0.19, 0.33, and 0.71 from T1 to T4, matching the vitality decline process of infested trees. Therefore, we considered the 2nd derivative at 530 nm to be a better indicator of infestation than at 715 nm, and to have a high potential to be the indicator of infestation stages.

Many bands in SWIR1 region had high separability at T2 and T3 e.g. 0.57 at 1280 nm at T2, 0.60 at 1092 nm and 1168 nm at T3. The separability was higher than the VNIR bands, but the consistency was low over time i.e. separability decreased with longer infestation times.

To sum up, the highest separability of healthy and infested trees at T4 was shown to be the 2nd derivative of the 530 nm wavelength (0.71), followed by the 1st derivative of the 552 nm wavelength (0.67). The result highlighted the sensitivity of green shoulder bands. The red edge bands also showed good separability at the 2nd derivative of the 715 nm wavelength (0.65), reflectance at 765 nm (0.65), 1st derivative of the 722 nm wavelength (0.58), reflectance at 710 nm (0.52), illustrating good potential of red edge bands for the early identification of infestations. These two regions, green shoulder and red edge, also showed relatively high separability at T2 (0.45 and 0.32, for green shoulder and

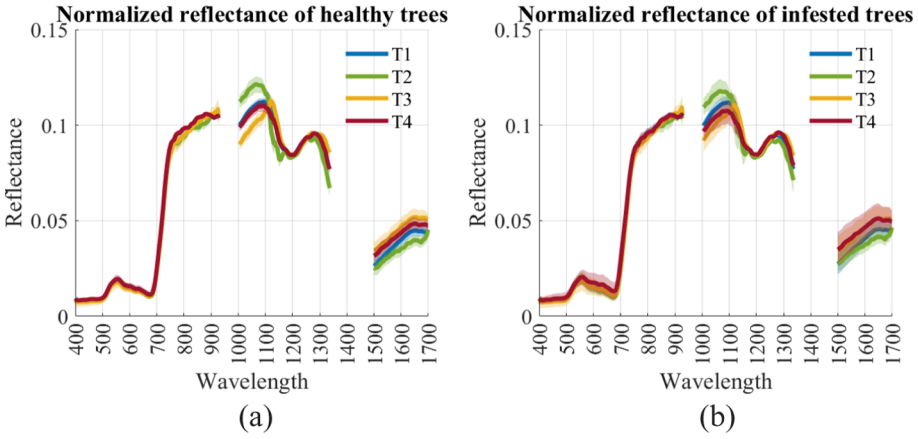

Fig. 5. Spectral curves of (a) healthy and (b) infested trees at different dates. The solid lines are the average reflectance and the shadows are the range of sampled trees.

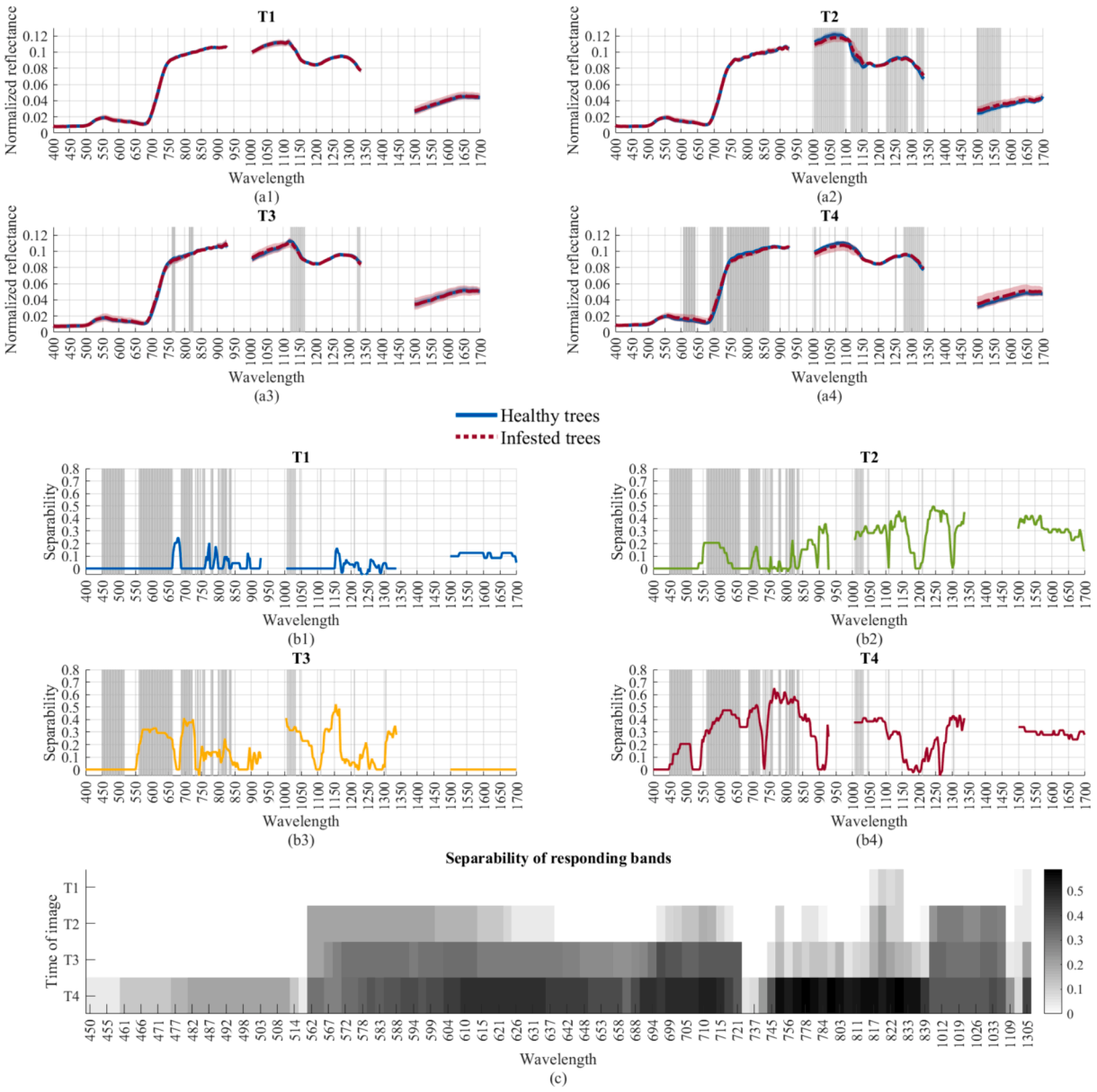

Fig. 6. (a) Reflectance curves and (b) the separability of each spectral band from healthy and attacked trees at T1 (a1, b1), T2 (a2, b2), T3 (a3, b3), and T4 (a4, b4), and (c) a heatmap of the separability of the responding bands. Grey lines in (a) mark the wavelengths with significant differences ($p < 0.01$ in a two-sided Wilcoxon rank-sum test) between healthy and attacked trees, and in (b) mark the wavelengths with increasing separability from T1 to T4.

red edge, respectively) and T3 (0.58 and 0.49, for green shoulder and red edge, respectively) compared to the other bands.

Many NIR and SWIR bands showed higher separability than the visible and red edge bands at T2 or T3, especially the 2nd derivative reflectance from SWIR1 bands. However, the separability decreased with longer infestation times. One possible reason could be that SWIR bands were sensitive to illumination conditions, so they contained additional noise information. Another possible reason could be that SWIR bands were sensitive to the tree defense reaction (e.g. releasing resin to trap bark beetles) at the beginning of the attacks until the colonization succeeded.

4.3. Green shoulder Inflection Point and green shoulder Curvature Point

4.3.1. Green shoulder Inflection Point and green shoulder Curvature Point

Both healthy and infested trees had increasing reflectance with longer wavelength in the green shoulder region, with two peaks for 1st derivative curves and one valley for the 2nd derivative curves. However, the slope and curvature of the spectral signatures were different between healthy and infested trees (Fig. 9). Compared to healthy ones, trees with longer infestation times had bigger slopes for the second Green Shoulder Inflection Point (GSIP, Fig. 9a) i.e. larger values of 1st derivatives at $GSIP_{545}$ (Fig. 9b). Spectral curves from the infested trees also had smaller curvatures at the Green Shoulder Curvature Point (GSCP) i.e. smaller absolute values of 2nd derivatives at $GSCP_{530}$ (Fig. 9c).

Fig. 10 shows the distribution of $GSIP_{520}$ and $GSCP_{530}$ for healthy and infested trees from T1 to T4. At T1 and T2, the three points of healthy and infested trees were distributed at similar wavelengths and derivative values. At T3 and T4, $GSIP_{520}$ for infested trees decreased slightly, while $GSIP_{545}$ and $GSCP_{530}$ increased compared to those of the healthy trees. At T4, the $GSCP_{530}$ of healthy and infested trees were greatly separated. These three points did not show a clear trend of shifting the wavelengths after infestation (Fig. 10a, 10b, 10c). The scatter plot (Fig. 10d) of $GSCP_{530}$ vs. the ratio of $GSIP_{545}$ and $GSIP_{520}$ showed a clear trend of the indices for infested trees separating from the healthy ones from T2 to T4.

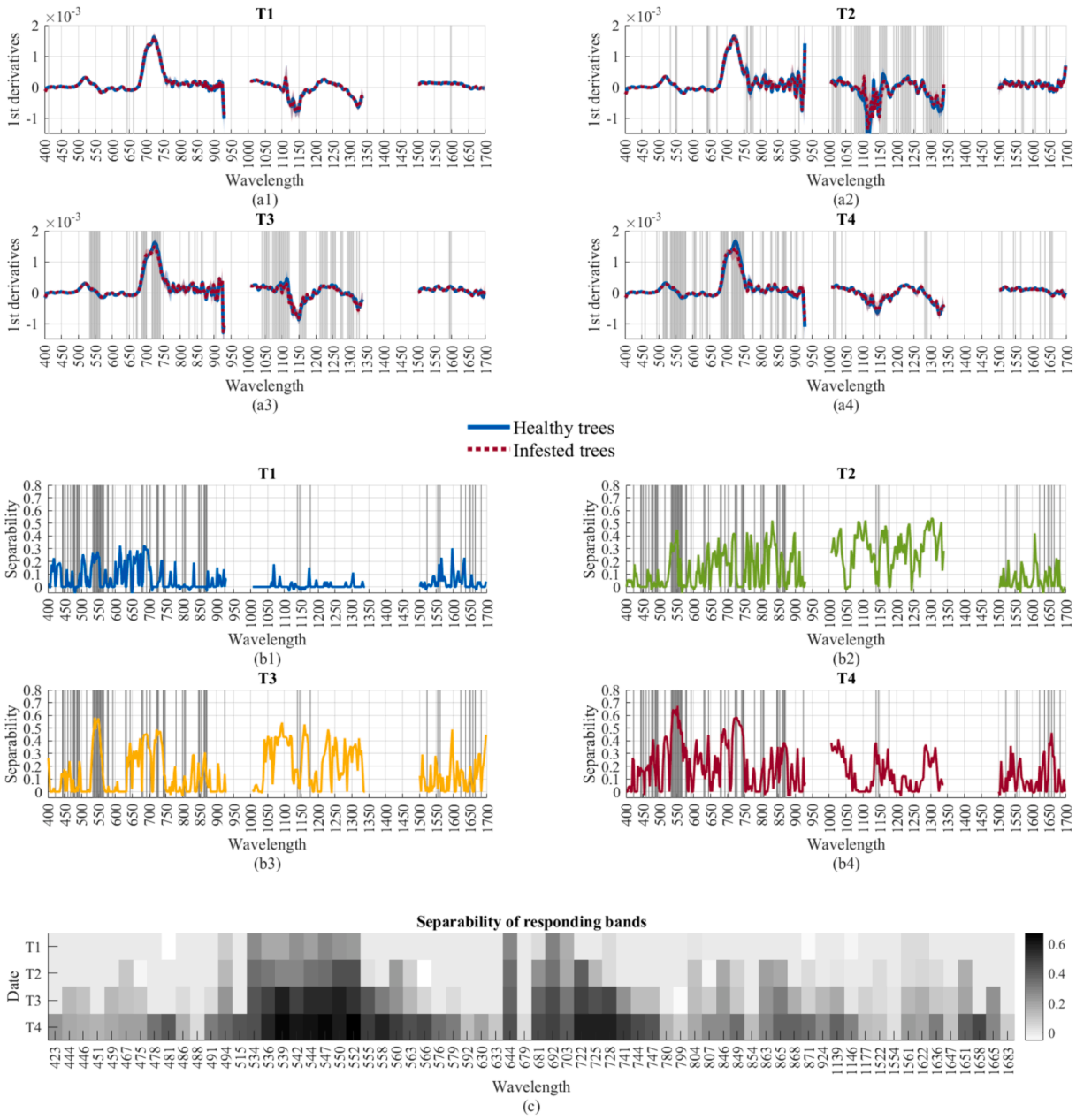

Fig. 7. (a) First derivative reflectance curves and (b) the separability of healthy and attacked trees at T1 (a1, b1), T2 (a2, b2), T3 (a3, b3), and T4 (a4, b4), and (c) a heatmap of the separability of the responding bands. Grey lines in (a) figures mark the wavelengths with significant differences between healthy and attacked trees, and in (b) figures mark the wavelengths with increasing separability from T1 to T4.

4.3.2. *Green shoulder indices*

When comparing the green shoulder VI values of a single tree over time, the values from healthy trees were more stable for GSCR1 and GSCR2, while most infested trees had increasing green shoulder VIs over time (Fig. 11 c1, d1). When normalizing these green shoulder VIs of individual trees by comparing them to the values from T1, the inner-group variation became smaller (Fig. 11, c2, d2). Table 6 shows the separability of the green shoulder VIs from healthy and attacked trees. $GSIP_{545}$ and GSCR1 showed around 0.2 separability at T1, which was unlikely to have been caused by ongoing infestation, while $GSIP_{520}$ and $GSCP_{530}$ had separability close to 0 at T1 and increased during T2 to T4. This illustrated that the LDA classification might be driven by the data from certain images, while not generic enough for images from different times. The detectability presented in Table 6 using thresholds derived from healthy trees in all images or using the δVIs (Eq. (5), gave solutions to the mentioned problem. It showed that infested trees at T1 and T2 still had VIs and δVIs within the healthy range, and the highest detectability was 0.36 at T3 and 0.80 at T4.

To simplify the green shoulder VIs using reflectance instead of derivatives, linear relationships were assumed and validated (Appendix). Then the classification using $GSCR1_{MS}$, $GSCR2_{MS}$, and their changes, respectively, were tested using the same method as above. After simplification, the green shoulder VIs obtained similar results as before simplification i.e. no separation of healthy and infested trees at T1 and T2, but the highest detectability of 0.43 at T3 and 0.80 at T4 (Fig. 11e, 11f, and Table 6).

4.4. *Comparing VIs*

Most VIs had higher separability for a single infestation time than the detectability using thresholds obtained from all infestation times (Table 7), showing their sensitivity to phenology or illumination

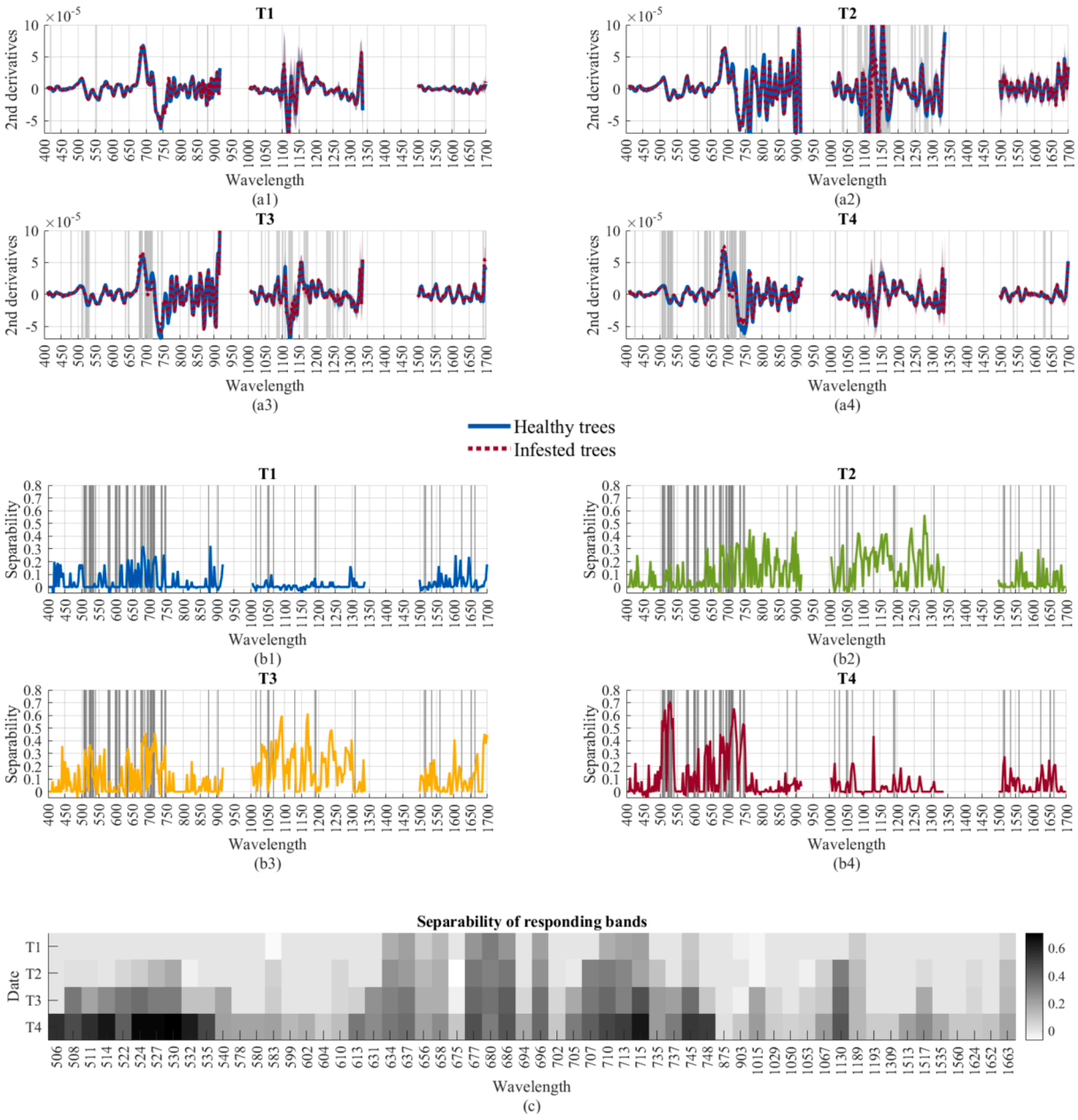

Fig. 8. (a) Second derivative reflectance curves and (b) the separability of healthy and attacked trees at T1 (a1, b1), T2 (a2, b2), T3 (a3, b3), and T4 (a4, b4), and (c) a heatmap of the separability of the responding bands. Grey lines in (a) figures mark the wavelengths with significant differences between healthy and attacked trees, and in (b) figures mark the wavelengths with increasing separability from T1 to T4.

conditions during the data acquisition. The detectability for both strategies, varying percentile and crown radii, were very low and unstable at T1 and T2 (around 0–0.2), and increased at T3 and T4. The PRI indices obtained the highest detectability, 0.43 at T3 and 0.70 at T4, followed by REIP with a detectability of 0.33 at T3 and 0.54 at T4, and followed by MR-DSWI1 with a detectability of 0.15 at T3 and 0.50 at T4 (Table 7). All the other VIs had detectability lower than 0.20 at T3 and 0.50 at T4, which indicated that it was challenging to early detect infestations. The VIs with SWIR bands such as DRS, DNII, and MSI, had relatively high separability around 0.3 at T2. However, the separability at T3 was 0, which might have been influenced by insufficient light during T3 image acquisition, making the detectability very low when using all times of images. This illustrated the potential of using SWIR bands for early detection, but it might be sensitive to the illumination factors.

5. Discussion

5.1. Spectral properties in the green region

This study highlighted the greater potential of the green shoulder over the green peak for the early identification of bark beetle infestations. It is common to use indices containing green peak reflectance to detect forest mortality, but the detection rates have been low when detecting green attacks. Results from this study illustrated that the spectrum around 530 nm contained more information relating to the tree health status than the green peak around 550 nm. Therefore, this study used the term ‘green shoulder’ instead of green to be more specific and highlight the ‘shoulder’ part of the green spectrum. In some studies, this same spectral region was also included as part of the green region or alternatively was called the ‘blue edge’ (Li et al., 2024; Zhang et al., 2019).

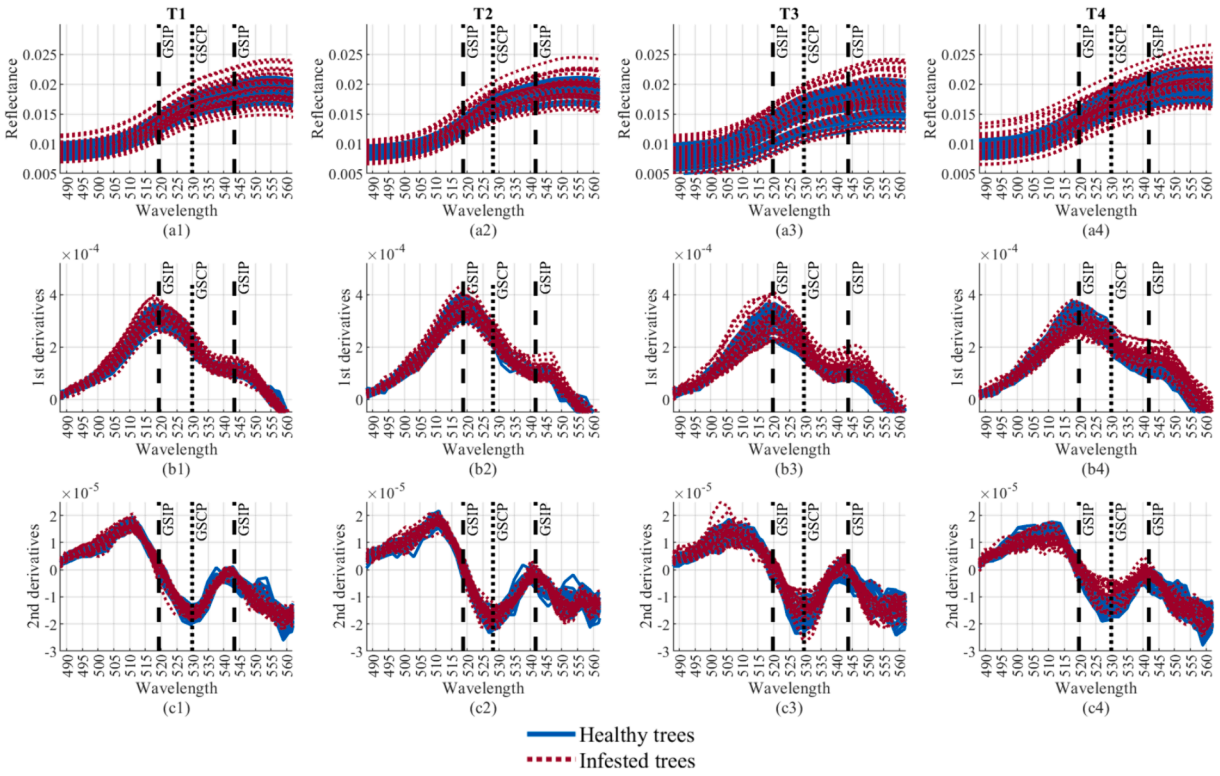

Fig. 9. (a) Green Shoulder Inflection Point and Green Shoulder Curvature Point shown on the reflectance curves, (b, c) 1st and 2nd derivative curves at T1 (a1, b1, c1), T2 (a2, b2, c2), T3 (a3, b3, c3), and T4 (a4, b4, c4). (For interpretation of the references to color in this figure legend, the reader is referred to the web version of this article.)

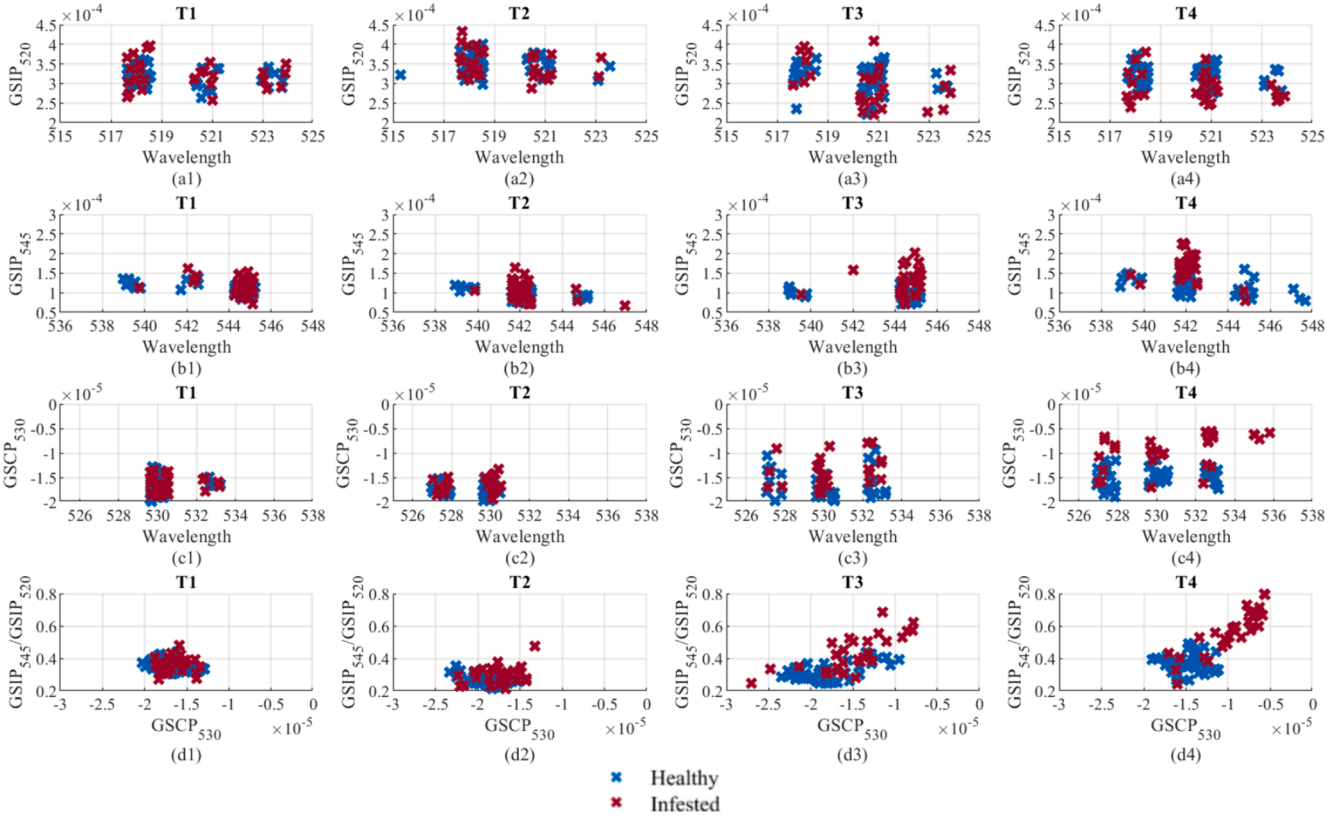

Fig. 10. (a) Distribution of the derivatives and wavelengths of $GSIP_{520}$, (b) $GSIP_{545}$, and (c) $GSCP_{530}$ of healthy and infested trees, and $GSCP_{530}$ vs. $GSIP_{545}$ / $GSIP_{520}$ at T1, T2, T3 and T4.

Table 6
Separability of healthy and infested trees and detectability of infested trees using different indices.

Indices	Separability				Detectability			
	T1	T2	T3	T4	T1	T2	T3	T4
$GSIP_{520}$	0.08	0.00	0.00	0.43	0.07	0.14	0.10	0.00
$GSIP_{545}$	0.17	0.25	0.55	0.59	0.03	0.03	0.24	0.62
$GSCP_{530}$	0.00	0.20	0.25	0.69	0.00	0.00	0.14	0.72
GSCR1	0.22	0.43	0.43	0.67	0.00	0.03	0.31	0.76
GSCR2	0.04	0.40	0.27	0.67	0.00	0.00	0.24	0.79
δGSCR1	0.00	0.44	0.49	0.76	0.00	0.00	0.28	0.83
δGSCR2	0.00	0.39	0.33	0.73	0.00	0.00	0.28	0.79
$GSCR1_{MS}$	0.29	0.44	0.52	0.70	0.00	0.00	0.38	0.79
$GSCR2_{MS}$	0.06	0.37	0.40	0.70	0.00	0.00	0.28	0.79
$δGSCR1_{MS}$	0.00	0.40	0.56	0.73	0.00	0.00	0.38	0.79
$δGSCR2_{MS}$	0.00	0.39	0.34	0.73	0.00	0.00	0.31	0.79

This study also proposed how to use the green shoulder spectrum. The indices were developed based on first and second derivative analysis instead of the reflectance, which improved detection compared to e.g. PRI developed using the reflectance. Compared to some previous studies that used the maximum derivatives in the green region (Li et al., 2024; Zhang et al., 2019; Peñuelas et al., 1994), this study decomposed the curves with two peaks. The minor peak, ignored in the past, was shown to be more sensitive to health decline than the major peak, and therefore showed better performance when used for stress detection.

Several studies in the 1990 s showed that the spectral signature in the green shoulder region was decidedly related to the photochemical functioning of the plant, such as photosynthetic efficiency and the epoxidation state of the xanthophyll cycle (EPS) (Peñuelas et al., 1994, 1995). Three components in the green region were highlighted in this study: 520 nm, 545 nm, and 530 nm. $GSIP_{520}$ was the point with the maximum 1st derivatives in the green region, which has been found to be correlated with diurnal photosynthetic rate and with seasonal chlorophyll and nitrogen changes (Peñuelas et al., 1994). $GSCP_{530}$ was the point with the minimum 2nd derivative in the green region, and its 2nd derivative was found to be correlated with water potential (Peñuelas et al., 1994). The wavelength 530 nm has also been used as the 'xanthophyll' wavelength (Peñuelas et al., 1994). The 545 nm component, corresponding to the minor peak of 1st derivative curves in the green region that shifted the most in this study, has had less attention in the past. Gamon et al. (1997) demonstrated the dominance of a 545 nm component in low incident photosynthetic photon flux density (PPFD). The 530 nm and 545 nm components were discovered by comparing the correlation with photosynthetic parameters band by band, while this study explained the selection of the wavelengths by derivative analysis.

Although many studies showed a positive correlation between PRI and light use efficiency (Garbulsky et al., 2011), the relationship is more

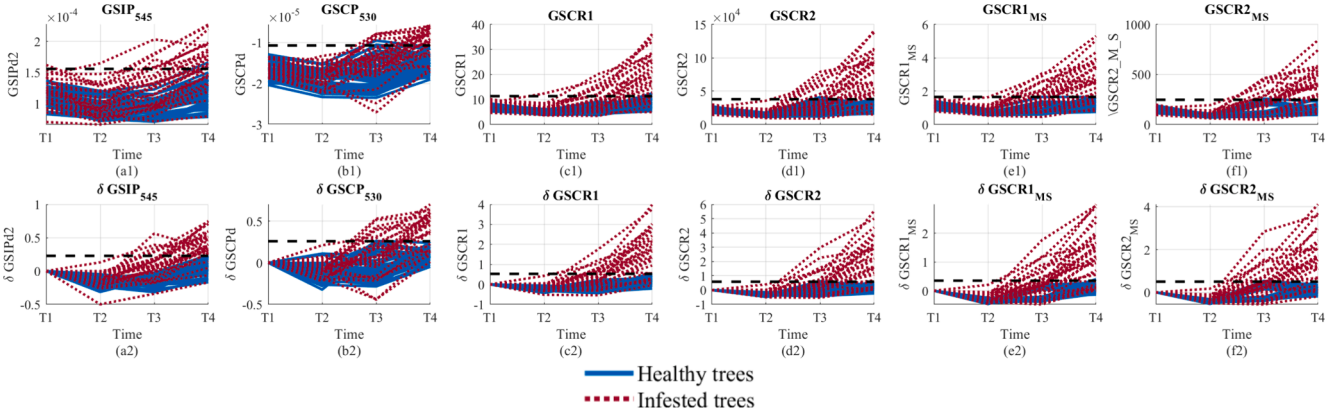

Fig. 11. Changes of $GSIP_{545}$ (a1), $GSCP_{530}$ (b1), GSCR1(c1), GSCR2 (d1), $GSCR1_{MS}$ (e1), $GSCR2_{MS}$ (f1) over time for healthy and infested trees and their difference compared to the T1 image (a2, b2, c2, d2, e2, f2).

Table 7
Separability and detectability using different vegetation indices (VIs). The VIs with relatively better performance are highlighted with a yellow background.

No.	Indices	Separability				Detectability			
		T1	T2	T3	T4	T1	T2	T3	T4
1	PRI 531/570	0.29	0.42	0.37	0.71	0.00	0.00	0.34	0.66
2	PRI 550/530	0.33	0.44	0.41	0.68	0.00	0.00	0.38	0.69
3	NGRDI	0.28	0.25	0.00	0.45	0.03	0.00	0.03	0.21
4	GLI	0.23	0.23	0.00	0.31	0.03	0.24	0.03	0.21
5	CIG	0.00	0.00	0.00	0.20	0.10	0.21	0.14	0.28
6	NDVI	0.00	0.00	0.00	0.27	0.10	0.21	0.14	0.28
7	CVI	0.00	0.00	0.12	0.22	0.00	0.00	0.10	0.00
8	ARI	0.00	0.00	0.12	0.68	0.03	0.00	0.17	0.00
9	GNDVI	0.00	0.04	0.17	0.29	0.17	0.21	0.21	0.31
10	MR-DSWI1	0.00	0.06	0.36	0.58	0.03	0.03	0.17	0.45
11	MR-DSWI2	0.00	0.06	0.36	0.61	0.03	0.03	0.17	0.34
12	MR-DSWI3	0.00	0.00	0.14	0.51	0.14	0.17	0.17	0.28
13	MR-DSWI4	0.00	0.00	0.10	0.54	0.14	0.14	0.17	0.24
14	NDRE	0.00	0.00	0.48	0.49	0.14	0.00	0.17	0.41
15	RVSI	0.00	0.39	0.00	−0.03	0.00	0.00	0.00	0.00
16	REIP	0.20	0.04	0.37	0.40	0.03	0.00	0.21	0.34
17	DRS	0.00	0.31	0.00	0.35	0.00	0.00	0.00	0.14
18	NDII	0.12	0.31	0.04	0.26	0.00	0.00	0.00	0.10
19	NDWI	0.00	0.00	0.00	0.42	0.00	0.10	0.00	0.00
20	MSI	0.12	0.29	0.00	0.35	0.00	0.00	0.00	0.10

complex in different stress conditions such as short-term or chronic stress, water or nutrient stress. In this study, the green shoulder indices, including PRI, increased during a longer infestation period, indicating physiological changes after being attacked by bark beetles. A study at the folia level showed larger PRI under nitrogen stress and lower PRI under water stress (Peñuelas et al., 1994). A study using airborne imagery at 2 m resolution showed that PRI increased with lower stem water potential, indicating larger water stress (Suárez et al., 2008). Studies have also shown that diurnal PRI is sensitive to the bidirectional reflectance distribution function (BRDF) of the aerial images and is greatly affected by atmospheric scattering, canopy structure and background (Suárez et al., 2008; Moncholi-Estornell et al., 2022). The green shoulder indices may also be sensitive to those factors and will need further investigation.

The results of this study also yielded a new methodology for vegetation stress detection, by detecting the photochemical adaptions (xanthophyll changes) when the stressor occurs, instead of waiting for the stress symptoms (chlorophyll and water content changes) that take some time to develop and appear. The xanthophyll-sensitive indices, including green shoulder indices and PRI, responded earlier than the chlorophyll-sensitive indices including red edge bands and water-sensitive indices including SWIR bands. In the past, insufficient attention has been paid to the adaptation of vegetation to stress, probably because of the limited time window when adaptions occur before mortality. This study achieved better detection, likely because of the capture of photosynthetic adaptions during frequent spectral acquisition. This new methodology needs to be further validated in more forests and environments.

5.2. Detectability of green attacks

In this study, we did not have field monitoring data on when individual trees were attacked, but the thermal sum data could be used to estimate the approximate time of the attack and brood development. The thermal sum was 800 dd to 1000 dd during weeks 27 to 29, when we could assume the trees were being attacked by the F1 filial generation. Based on this assumption, trees experienced 1–3 weeks of infestation at T1, 3–5 weeks at T2, 5–7 weeks at T3, and 7–9 weeks at T4. Visual interpretation of the RGB orthophotos and low separability of the visible bands confirmed that all the infested trees were in the green attack phase without discoloration from T1 to T4. Nevertheless, attacking time might differ between individual trees; therefore, this study could not specify the detectability to certain weeks of infestation but roughly estimated it. Another limitation of the study is the restricted study area and sample size, which were limited by the natural outbreak level. Therefore, this study could not analyze the variance in detectability from different stands, but only compare the results with other studies (Huo et al. 2023).

The infestation detectability was close to zero at T1 and T2, and then rapidly increased to around 0.4 at T3 and around 0.8 at T4. Occasionally, higher separability was shown when using some VIs or derivatives, but those VIs or derivatives showed lower separability at T3 and T4, indicating an inconsistency in capturing tree stress. The rapid change of the detectability during 5–9 weeks of infestation was consistent with a previous study in southern Sweden, where the detection rates of infested trees rapidly increased from 15 % to 90 % at five and ten weeks of infestation from the first swarming (Huo et al. 2023). The same study also pointed out lower detectability of trees attacked from the F1 filial generation, with only a detection rate of 67 % at 12 weeks of infestation. Compared to the previous study, this study obtained higher detection rates i.e. around 80 % during 7–9 weeks of infestation from the F1 filial generation. Three probable reasons can be considered. First, this study used hyperspectral imagery with narrower bands, which could be more sensitive to the decline in health than wider bands provided by multispectral cameras. Our results also showed higher detection rates using the simplified green shoulder indices with smaller bandwidths. Second, using green shoulder indices achieved higher detection rates compared to other VIs. The indices used 530 nm reflectance, which was not available in the multispectral data in the other study. Third, the trees in this study might experience higher intensity of attacks or lower vitality before the attacks, resulting in faster vitality decline. The two study areas in southern Sweden and southern Finland had similar thermal conditions, and both experienced drought and high temperatures in 2021. However, the forest in Sweden was managed actively, while the forest in Finland was in a nature reserve, and they might experience different severity of beetle outbreaks.

Using the developed method in this study, around 40 % and 80 % of trees could be detected and removed 5–7 and 7–9 weeks after the initial attack from the F1 filial generation. Although the detection rate was the highest compared to those presented in similar studies using airborne and drone imagery, the time window for detection and sanitation cutting was still very limited, bringing into doubt the feasibility of early detection and early removal for damage control using current remote sensing techniques. The low detectability observed from close to the ground also contradicted some studies that claimed pre-emergence detection using satellite images. With much lower resolution images, it is unlikely to detect green attacks e.g. in May in middle and southern Europe, and in June in northern Europe. As suggested by a critical review of recent research on early detection, field validation on the infestation stages is crucial to draw conclusions on how early remote sensing can detect infestations (Kautz et al., 2024).

5.3. Feasibility of forest health monitoring and damage control

Using hyperspectral drone images for pre-emergence detection is not directly feasible for practical use, given the high cost of the sensors and the limited area covered. However, although this study used hyperspectral data, it developed and proposed indices targeted to be used by multispectral sensors e.g. on small drones, airships, and satellites. The simplified indices only need three broad bands, and such sensors will be significantly lighter, providing increased acquisition capabilities for focused forest monitoring. For example, the hyperspectral drone system (448 bands) used in this project costs about eight times the multispectral drone system (8 bands) used by Huo et al. (2023), and about 50 times one of the commonly used multispectral drones (e.g. DJI Mavic 3, 4 bands). The hyperspectral drone system weighs almost 25 kg, while a 4-band multispectral drone such as DJI Mavic 3 weighs 335.5 g. The data acquisition and processing of hyperspectral images requires many more steps and much greater time than multispectral images. Therefore, developing methodologies using hyperspectral drone systems for the fundamental research but investigating sensitive bands and VIs using multispectral sensors is crucial for practical use.

Various platforms carrying sensors are also being developed to include automation and cost less, such as unmanned airships that can cover larger areas, and autonomous drones that can deploy from, and return to, self-contained stations with data downloading and processing functions. Compared to machine learning-based approaches, for instance, as described by Minarik et al., (2021), Junttila et al. (2022), Safonova et al., (2022) and Turkulainen et al., (2023), this study proposed VIs that can be implemented without requiring hyperspectral bands as input and without extensive training materials. This would facilitate the development of entirely unsupervised, direct analysis techniques for detecting bark beetle green attacks.

This study proposed the use of an additional band at 530 nm, which has not been commonly covered by satellite images thus far, but is covered by the Planetscpe SuperDove satellite images available from 2022 with the additional band Green 1 (centered at 531 nm with 36 nm bandwidth, 3.7 m resolution) (Dalponte et al., 2023). Further studies are needed to test the robustness of the green shoulder indices on different datasets and acquired from different sensors, including the Planetscope superDove images. If they result in a stable performance, the Green 1 band could be used by more satellites, contributing to the large-area monitoring of forest disturbances under a changing climate. For large-

area monitoring of early bark beetle infestation symptoms, the spatial and spectral resolution of satellite images are still limiting factors at present. However, satellite sensors are also being developed with higher spatial resolutions and a greater band coverage e.g. the WorldView-3 multispectral images with 0.31 m resolution (Yu et al., 2020), middle-resolution hyperspectral satellite EnMAP (Stuffler et al., 2007) and PRISMA (Cogliati et al., 2021).

6. Conclusions

This study tested the detectability of trees affected by green attack using hyperspectral images with narrow bands and high resolution in the spectral range of 400–1700 nm. We discovered that the peak and valley points of the first and second derivative curves in the green shoulder spectral region consistently shift with longer infestation times. Using suggested green shoulder indices based on the calculation of green shoulder inflection and curvature points, more infested trees can be detected compared to using other VIs including commonly used red edge indices. The proposed indices could also be simplified by the combination of three bands: blue (490 nm), green (550 nm), and green 1 (530 nm). These could be potentially used with multispectral cameras at a lower cost without obviously sacrificing detection rates. The results were consistent with studies showing spectral features in the green shoulder region being sensitive to the xanthophyll cycle during photosynthesis and its changes under nutrition stress.

Using the indices developed in this study, a detectability of 0, 0.3, and 0.8 during 3–5, 5–7, and 7–9 weeks of infestation was achieved i.e. pre-emergence detection using hyperspectral drone images. The detectability was higher than that recorded in any other similar studies with field validation, while the time window for removing the infested trees was still limited. This study also highlighted the potential of tracking photosynthesis adaptions in early stress detection. More case studies from different regions and different thermal conditions are needed to verify the superiority of hyperspectral drone images in detecting infestations. More studies are needed to explore further the methodology of using red edge, NIR, and SWIR bands with such a hyperspectral drone system.

CRediT authorship contribution statement

Langning Huo: Writing – review & editing, Writing – original draft, Visualization, Validation, Project administration, Methodology, Investigation, Funding acquisition, Formal analysis, Conceptualization. **Niko Koivumäki:** Writing – review & editing, Resources, Data curation. **Raquel A. Oliveira:** Writing – review & editing, Resources. **Teemu Hakala:** Writing – review & editing, Resources. **Lauri Markelin:** Writing – review & editing, Resources. **Roope Näsi:** Writing – review & editing, Resources. **Juha Suomalainen:** Writing – review & editing, Resources. **Antti Polvivaara:** Writing – review & editing, Resources. **Samuli Junttila:** Writing – review & editing, Resources. **Eija Honkavaara:** Writing – review & editing, Supervision, Resources, Project administration, Funding acquisition, Data curation, Conceptualization.

Declaration of competing interest

The authors declare that they have no known competing financial interests or personal relationships that could have appeared to influence the work reported in this paper.

Acknowledgment

The project is funded by the Swedish Governmental Agency for Innovation Systems Vinnova (project no. 2022-01218), the Forest Damage Center at the Swedish University of Agricultural Sciences (projects no. 260FDC57 and 260FDC44), the European Union with project RESDINET (no. 101078970), Academy of Finland under grants 355612, 357380, 353264, and 353262, the Ministry of Agriculture and Forestry of Finland with the projects MONITUHO (no. 647/03.02.06.00/2018), SPRUCERISK (no. VN/5292/2021), and MMM_UNITE (no. VN/3482/2021). This study was affiliated with the Academy of Finland Flagship Forest–Human–Machine Interplay–Building Resilience, Redefining Value Networks and Enabling Meaningful Experiences (UNITE) (decision no. 337127).

Appendix

Validation of the linear relationships proposed in Eqs. (7)–(11) is shown in Figure 12, which also shows R^2.

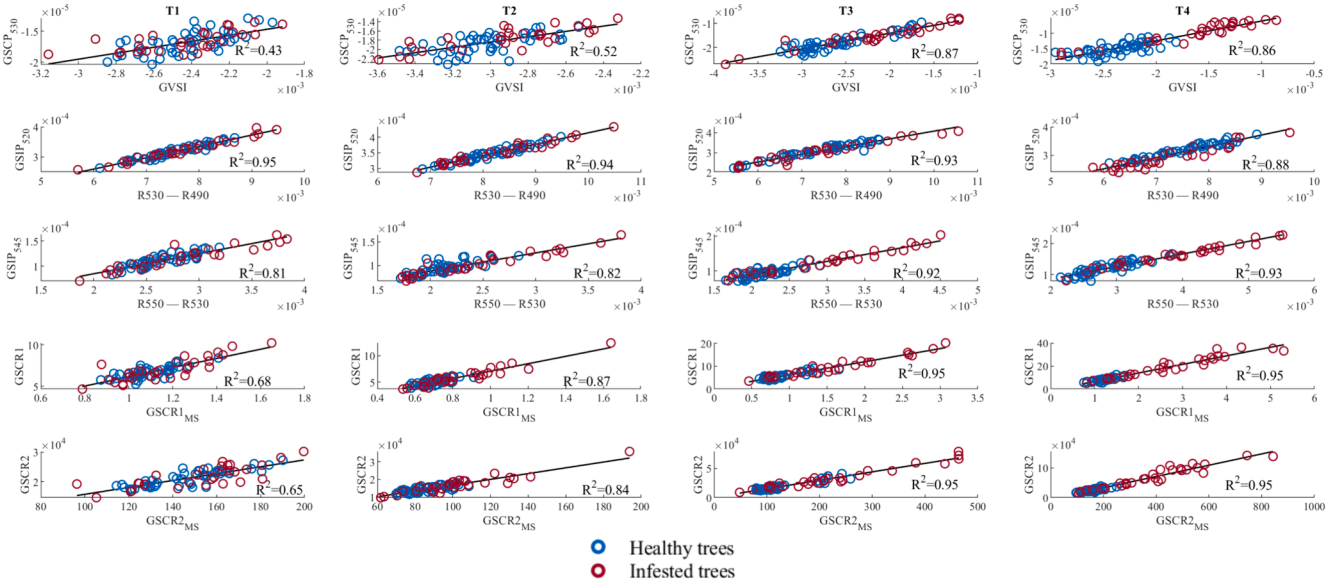

Fig. 12. Linear relationships proposed in Equations .

References

Abdullah, H., Darvishzadeh, R., Skidmore, A.K., Groen, T.A., Heurich, M., 2018. European spruce bark beetle (Ips typographus, L.) green attack affects foliar reflectance and biochemical properties. Int. J. Appl. Earth Obs. Geoinf. 64, 199–209.

Abdullah, H., Skidmore, A.K., Darvishzadeh, R., Heurich, M., 2019. Sentinel-2 accurately maps green-attack stage of European spruce bark beetle (Ips typographus L.) compared with Landsat-8. Remote Sens. Ecol. Conserv. 5, 87–106.

Annila, E. (1969). Influence of temperature upon the development and voltinism of Ips typographus L. (Coleoptera, Scolytidae). *Annales Zoologici Fennici*, *6*. http://www.jstor.org/stable/23731366.

Barnes, E.M., Clarke, T.R., Richards, S.E., Colaizzi, P.D., Haberland, J., Kostrzewski, M., Waller, P., Choi, C., Riley, E., Thompson, T., Lascano, R.J., Li, H., & Moran, M.S. (Eds.) (2000). Coincident Detection of Crop Water Stress, Nitrogen Status, and Canopy Density Using Ground-Based Multispectral Data.

Bárta, V., Lukeš, P., Homolová, L., 2021. Early detection of bark beetle infestation in Norway spruce forests of Central Europe using Sentinel-2. Int. J. Appl. Earth Obs. Geoinf. 100, 102335.

Bárta, V., Hanuš, J., Dobrovolný, L., Homolová, L., 2022. Comparison of field survey and remote sensing techniques for detection of bark beetle-infested trees. For. Ecol. Manage. 506, 119984.

Battisti, A., Larsson, S., 2023. Climate change and forest insect pests. In: Allison, J.D., Paine, T.D., Slippers, B., Wingfield, M.J. (Eds.), Forest Entomology and Pathology. Springer International Publishing, Cham, pp. 773–787.

Cogliati, S., Sarti, F., Chiarantini, L., Cosi, M., Lorusso, R., Lopinto, E., Miglietta, F., Genesio, L., Guanter, L., Damm, A., Pérez-López, S., Scheffler, D., Tagliabue, G., Panigada, C., Rascher, U., Dowling, T.P.F., Giardino, C., Colombo, R., 2021. The PRISMA imaging spectroscopy mission: overview and first performance analysis. Remote Sens. Environ. 262, 112499.

Dalponte, M., Cetto, R., Marinelli, D., Andreatta, D., Salvadori, C., Pirotti, F., Frizzera, L., Gianelle, D., 2023. Spectral separability of bark beetle infestation stages: A single-tree time-series analysis using Planet imagery. Ecol. Ind. 153, 110349.

Dobor, L., Hlásny, T., Rammer, W., Zimová, S., Barka, I., Seidl, R., 2020. Is salvage logging effectively dampening bark beetle outbreaks and preserving forest carbon stocks? J. Appl. Ecol. 57, 67–76.

Estrada, J.S., Fuentes, A., Reszka, P., Auat Cheein, F., 2023. Machine learning assisted remote forestry health assessment: a comprehensive state of the art review. Front. Plant Sci. 14, 1139232.

Fassnacht, F.E., Latifi, H., Ghosh, A., Joshi, P.K., Koch, B., 2014. Assessing the potential of hyperspectral imagery to map bark beetle-induced tree mortality. Remote Sens. Environ. 140, 533–548.

Fora, C.G., Balog, A., 2021. The effects of the management strategies on spruce bark beetles populations (Ips typographus and Pityogenes chalcographus), in apuseni natural park romania. *Forests* 12, 760.

Gamon, J.A., Serrano, L., Surfus, J.S., 1997. The photochemical reflectance index: an optical indicator of photosynthetic radiation use efficiency across species, functional types, and nutrient levels. Oecologia 112, 492–501.

Garbulsky, M.F., Peñuelas, J., Gamon, J., Inoue, Y., Filella, I., 2011. The photochemical reflectance index (PRI) and the remote sensing of leaf, canopy and ecosystem radiation use efficienciesA review and meta-analysis. Remote Sens. Environ. 115, 281–297.

Anatoly A. Gitelson, M. N. Merzlyak, Y. Zur, R. Stark, & and U. Gritz (Eds.) (2001). Non-destructive and remote sensing techniques for estimation of vegetation status.

Gitelson, A.A., Merzlyak, M.N., Lichtenthaler, H.K., 1996. Detection of red edge position and chlorophyll content by reflectance measurements near 700 nm. J. Plant Physiol. 148, 501–508.

Gitelson, A.A., Gritz, Y., Merzlyak, M.N., 2003. Relationships between leaf chlorophyll content and spectral reflectance and algorithms for non-destructive chlorophyll assessment in higher plant leaves. J. Plant Physiol. 160, 271–282.

Guyot, G., Baret, F., Major, D.J., 1988. High spectral resolution: Determination of specral shifts between the red and the near infrared. International Archives of Photogrammetry and Remote Sensing 11.

Hardisky, M.A., Klemas, V., & Smart, R.M. (1983). The Influence of Soil Salinity, Growth Form, and Leaf Moisture on-the Spectral Radiance of Spartina alterniflora Canopies, Photogrammetry Engineering and Remote Sensing *Vol. 49, No. 1*.

Honkavaara, E., Näsi, R., Oliveira, R., Viljanen, N., Suomalainen, J., Khoramshahi, E., Hakala, T., Nevalainen, O., Markelin, L., Vuorinen, M., Kankaanhuhta, V., Lyytikäinen-Saarenmaa, P., Haataja, L., 2020. Using multitemporal hyper- and multispectral UAV imaging for detecting bark beetle infestation on norway spruce. *Int. Arch. Photogramm. Remote. Sens. Spat. Inf. Sci.* 429–434. XLIII-B3-2020.

Huntjr, E., Rock, B., 1989. Detection of changes in leaf water content using Near- and Middle-Infrared reflectances☆. Remote Sens. Environ. 30, 43–54.

Huo, L., Persson, H.J., Lindberg, E., 2021. Early detection of forest stress from European spruce bark beetle attack, and a new vegetation index: Normalized distance red & SWIR (NDRS). Remote Sens. Environ. 255, 112240.

Huo, L., Persson, H.J., Bohlin, J., Lindberg, E. (Eds.), 2023. Green Attack or Overfitting? Comparing Machine-Learning- and Vegetation-Index-Based Methods to Early Detect European Spruce Bark Beetle Attacks Using Multispectral Drone Images. IEEE.

Huo, L., Lindberg, E., Bohlin, J., Persson, H.J., 2023. Assessing the detectability of European spruce bark beetle green attack in multispectral drone images with high spatial- and temporal resolutions. Remote Sens. Environ. 287, 113484.

Jackson, T.J., Chen, D., Cosh, M., Li, F., Anderson, M., Walthall, C., Doriaswamy, P., Hunt, E.R., 2004. Vegetation water content mapping using Landsat data derived normalized difference water index for corn and soybeans. Remote Sens. Environ. 92, 475–482.

Jamali, S., Olsson, P.-O., Ghorbanian, A., Müller, M., 2023. Examining the potential for early detection of spruce bark beetle attacks using multi-temporal Sentinel-2 and harvester data. ISPRS J. Photogramm. Remote Sens. 205, 352–366.

Junttila, S., Näsi, R., Koivumäki, N., Imangholiloo, M., Saarinen, N., Raisio, J., Holopainen, M., Hyyppä, H., Hyyppä, J., Lyytikäinen-Saarenmaa, P., Vastaranta, M., Honkavaara, E., 2022. Multispectral imagery provides benefits for mapping spruce tree decline due to bark beetle infestation when acquired late in the season. Remote Sens. (Basel) 14, 909.

Kärvemo, S., Huo, L., Öhrn, P., Lindberg, E., Persson, H.J., 2023. Different triggers, different stories: Bark-beetle infestation patterns after storm and drought-induced outbreaks. For. Ecol. Manage. 545, 121255.

Kautz, M., Feurer, J., Adler, P., 2024. Early detection of bark beetle (Ips typographus) infestations by remote sensing – A critical review of recent research. For. Ecol. Manage. 556, 121595.

Knoke, T., Gosling, E., Thom, D., Chreptun, C., Rammig, A., Seidl, R., 2021. Economic losses from natural disturbances in Norway spruce forests – A quantification using Monte-Carlo simulations. Ecol. Econ. 185, 107046.

Latowski, D., Kuczyńska, P., Strzałka, K., 2011. Xanthophyll cycle–a mechanism protecting plants against oxidative stress. Redox Report : Communications in Free Radical Research 16, 78–90.

Li, N., Huo, L., Zhang, X., 2022. Classification of pine wilt disease at different infection stages by diagnostic hyperspectral bands. Ecol. Ind. 142, 109198.

Li, N., Huo, L., Zhang, X., 2024. Using only the red-edge bands is sufficient to detect tree stress: A case study on the early detection of PWD using hyperspectral drone images. Comput. Electron. Agric. 217, 108665.

Louhaichi, M., Borman, M.M., Johnson, D.E., 2001. Spatially located platform and aerial photography for documentation of grazing impacts on wheat. Geocarto Int. 16, 65–70.

Luo, Y., Huang, H., Roques, A., 2022. Early monitoring of forest wood-boring pests with remote sensing. Annu. Rev. Entomol.

Marvasti-Zadeh, S.M., Goodsman, D., Ray, N., Erbilgin, N., 2024. Early detection of bark beetle attack using remote sensing and machine learning: A review. ACM Comput. Surv. 56, 1–40.

Merton, R.N., 1998. Monitoring community hysteresis using spectral shift analysis and the red-edge vegetation stress index. Seventh Annual JPL Airborne Earth Science Workshop.

Meurant, G. (Ed.), 1999. Studies in Mathematics and Its Applications : Computer Solution of Large Linear Systems. Elsevier.

Minařík, R., Langhammer, J., Lendzioch, T., 2021. Detection of bark beetle disturbance at tree level using UAS multispectral imagery and deep learning. Remote Sens. (Basel) 13, 4768.

Moncholi-Estornell, A., van Wittenberghe, S., Cendrero-Mateo, M.P., Alonso, L., Malenovský, Z., Moreno, J., 2022. Impact of Structural, Photochemical and Instrumental Effects on Leaf and Canopy Reflectance Variability in the 500–600 nm Range. Remote Sens. (Basel) 14, 56.

Öhrn, P., Långström, B., Lindelöw, Å., Björklund, N., 2014a. Seasonal flight patterns of Ips typographus in southern S weden and thermal sums required for emergence. Agric. For. Entomol. 16, 147–157.

Öhrn, P., Långström, B., Lindelöw, Å., Björklund, N., 2014b. Seasonal flight patterns of Ips typographus in southern Sweden and thermal sums required for emergence. Agric. For. Entomol. 16, 147–157.

Olsson, P.-O., Bergman, H., Piltz, K., 2023. Exploring the potential to use in-between pixel variability for early detection of bark beetle attacked trees. AGILE: Giscience Series 4, 1–6.

Peguero-Pina, J.J., Morales, F., Flexas, J., Gil-Pelegrín, E., Moya, I., 2008. Photochemistry, remotely sensed physiological reflectance index and de-epoxidation state of the xanthophyll cycle in quercus coccifera under intense drought. Oecologia 156. http://www.jstor.org/stable/40213222.

Peñuelas, J., Gamon, J.A., Fredeen, A.L., Merino, J., Field, C.B., 1994. Reflectance indices associated with physiological changes in nitrogen- and water-limited sunflower leaves. Remote Sens. Environ. 48, 135–146.

Peñuelas, J., Filella, I., Gamon, J.A., 1995. Assessment of photosynthetic radiation-use efficiency with spectral reflectance. New Phytol. 131, 291–296.

Persson, H.J., Kärvemo, S., Lindberg, E., Huo, L., 2024. Large-scale wall-to-wall mapping of bark beetle damage and forest practices using the distance red swir index and operational harvester data. Ecological Indicators 162, 112036.

Pureswaran, D.S., Roques, A., Battisti, A., 2018. Forest insects and climate change. Current Forestry Reports 4, 35–50.

Rouse, J., R. Haas, J. Schell, & D. Deering (Eds.) (1973). Monitoring Vegetation Systems in the Great Plains with ERTS.

Safonova, A., Hamad, Y., Alekhina, A., Kaplun, D., 2022. Detection of norway spruce trees (Picea Abies) infested by bark beetle in UAV images using YOLOs architectures. IEEE Access 10, 10384–10392.

Stuffler, T., Kaufmann, C., Hofer, S., Förster, K.P., Schreier, G., Mueller, A., Eckardt, A., Bach, H., Penné, B., Benz, U., Haydn, R., 2007. The EnMAP hyperspectral imager—An advanced optical payload for future applications in Earth observation programmes. Acta Astronaut. 61, 115–120.

Suárez, L., Zarco-Tejada, P.J., Sepulcre-Cantó, G., Pérez-Priego, O., Miller, J.R., Jiménez-Muñoz, J.C., Sobrino, J., 2008. Assessing canopy PRI for water stress detection with diurnal airborne imagery. Remote Sens. Environ. 112, 560–575.

Trubin, A., Kozhoridze, G., Zabihi, K., Modlinger, R., Singh, V.V., Surový, P., Jakuš, R., 2023. Detection of susceptible norway spruce to bark beetle attack using planetscope multispectral imagery. Frontiers in Forests and Global Change 6, 87.

Tsai, F., Philpot, W., 1998. Derivative analysis of hyperspectral data. Remote Sens. Environ. 66, 41–51.

Tucker, C.J., 1979. Red and photographic infrared linear combinations for monitoring vegetation. Remote Sens. Environ. 8, 127–150.
Turkulainen, E., Honkavaara, E., Näsi, R., Oliveira, R.A., Hakala, T., Junttila, S., Karila, K., Koivumäki, N., Pelto-Arvo, M., Tuviala, J., Östersund, M., Pölönen, I., Lyytikäinen-Saarenmaa, P., 2023. Comparison of deep neural networks in the classification of bark beetle-induced spruce damage using UAS images. Remote Sens. (Basel) 15, 4928.
Vilfan, N., van der Tol, C., Yang, P., Wyber, R., Malenovský, Z., Robinson, S.A., Verhoef, W., 2018. Extending Fluspect to simulate xanthophyll driven leaf reflectance dynamics. Remote Sens. Environ. 211, 345–356.
Vincini, M., Frazzi, E., D'Alessio, P., 2008. A broad-band leaf chlorophyll vegetation index at the canopy scale. Precis. Agric. 9, 303–319.
Wermelinger, B., 2004. Ecology and management of the spruce bark beetle Ips typographus—a review of recent research. For. Ecol. Manage. 202, 67–82.
Zabihi, K., Surovy, P., Trubin, A., Singh, V.V., Jakuš, R., 2021. A review of major factors influencing the accuracy of mapping green-attack stage of bark beetle infestations using satellite imagery: Prospects to avoid data redundancy. Remote Sens. Appl.: Soc. Environ. 24, 100638.
Zahir, S.A.D.M., Omar, A.F., Jamlos, M.F., Azmi, M.A.M., Muncan, J., 2022. A review of visible and near-infrared (Vis-NIR) spectroscopy application in plant stress detection. Sens. Actuators, A 338, 113468.
Zhang, C., Ren, H., Dai, X., Qin, Q., Li, J., Zhang, T., Sun, Y., 2019. Spectral characteristics of copper-stressed vegetation leaves and further understanding of the copper stress vegetation index. Int. J. Remote Sens. 40, 4473–4488.